Journal of Alloys and Compounds 1035 (2025) 181339

Contents lists available at ScienceDirect

Journal of Alloys and Compounds

journal homepage: www.elsevier.com/locate/jalcom

Eutectic orientation relationships in Sn-Bi solder

X. Shen *, A. Zois, J.O. Douglas, C.M. Gourlay

Department of Materials, Imperial College London, London SW7 2AZ, UK

ARTICLE INFO

Keywords:
Eutectic solidification
Microstructure formation
Orientation relationship
Interfaces
Low temperature solder

ABSTRACT

The Sn-Bi eutectic is used increasingly as a low temperature solder (LTS) in electronics manufacturing. Here, we measure eutectic orientation relationships (ORs) in Sn-58Bi and compare the ORs formed during solidification of undercooled solder balls with those from unidirectional solidification. In both solidification conditions, three ORs formed, each involving $\{01\bar{1}2\}$ as the main interface planes in (Bi) with different interface planes in β-Sn. In each OR, the eutectic bismuth was commonly twinned, with multiple (Bi) orientations related to each β-Sn orientation which is explained in terms of the orientation variants of the ORs and the twin variants in (Bi). It is found that the dominant eutectic OR changes as the nucleation undercooling becomes deeper in solder balls which is discussed in terms of the effects of undercooling on the fraction of tin dendrites and the eutectic growth velocity. The ability to change the dominant eutectic OR may provide a pathway to control interfaces between the β-Sn and (Bi) phases which play an important role in the reliability of Sn-58Bi joints.

1. Introduction

In recent years, there has been high interest in using alloys of Sn-Bi eutectic composition as low temperature solders to reduce soldering defects caused by dynamic warpage and protect temperature-sensitive components [1–3]. The low eutectic temperature of ~138°C [4,5] enables peak reflow temperatures in the range 160°C - 190°C [6–9], and has shown promise at meeting the environmental, economic, and design requirements of low temperature soldering and hybrid soldering [6,10,11]. Recent research has suggested that Sn-Bi solders provide adequate joint strength, creep strength and cost-effectiveness in addition to lowering the thermal stresses and protecting from damage on printed wiring boards [12–16]. However, eutectic Sn-Bi solder can be prone to brittle fracture due to the high volume fraction (around 50 vol%) of brittle (Bi) phase that limits its use in mobile computing applications [12,17].

In Sn-58Bi solder, a eutectic microstructure occupies the majority of the volume and is responsible for much of the electrical and mechanical properties. Of particular importance are the interfaces between the β-Sn and (Bi) phases since the crack path in thermal fatigue is typically along β-Sn/(Bi) interfaces [18]. These interfaces initially form during eutectic solidification and continue to develop as the microstructure evolves in service. While past work has studied the factors affecting the morphology and length scale of the Sn-Bi eutectic over many years [19–25], to our knowledge, past studies have not measured the orientation relationships and interfaces formed by Sn-Bi eutectic solidification. Such information is needed to better understand failure mechanisms in Sn-Bi solders and could be used to control the β-Sn/(Bi) interfaces formed in Sn-Bi solder joint solidification.

One area where (Bi)/β-Sn interfaces and orientation relationships have been studied is in the solid-state precipitation of (Bi) from supersaturated solid solution of β-Sn, usually in alloys with relatively low Bi concentration [26–30]. These studies have shown that (Bi) precipitates are usually plates aligned at constant crystallographic orientation in the β-Sn matrix [26,27]. Belyakov et al. [29] measured two crystallographic orientation relationships (ORs) between the β-Sn matrix and (Bi) precipitates in Sn-3Ag-0.5Cu-4Bi after solid-state precipitation, which they denoted OR-1 and OR-2 as follows:

$$\mathrm{OR}-1: \quad \{100\}_{\beta-\mathrm{Sn}} \parallel \{01\bar{1}2\}_{(\mathrm{Bi})} \ \& < 010 >_{\beta-\mathrm{Sn}} \parallel < 2\bar{2}01 >_{(\mathrm{Bi})}$$

$$\mathrm{OR}-2: \quad \{100\}_{\beta-\mathrm{Sn}} \parallel \{01\bar{1}2\}_{(\mathrm{Bi})} \ \& < 011 >_{\beta-\mathrm{Sn}} \parallel < 2\bar{2}01 >_{(\mathrm{Bi})}$$

The current paper explores eutectic ORs in Sn-58Bi and compares them with the ORs measured by Belyakov et al. [29] for solid state precipitation in Sn-3Ag-0.5Cu-4Bi.

First, it is instructive to briefly overview the crystal structures of the (Bi) and β-Sn phases and some similarities between them that will be used to interpret the crystallographic measurements later in the paper. The lattice parameters are summarised in Table 1 where the

* Corresponding author.
E-mail address: x.shen20@imperial.ac.uk (X. Shen).

https://doi.org/10.1016/j.jallcom.2025.181339
Received 21 March 2025; Received in revised form 16 May 2025; Accepted 31 May 2025
Available online 2 June 2025
0925-8388/© 2025 The Authors. Published by Elsevier B.V. This is an open access article under the CC BY license (http://creativecommons.org/licenses/by/4.0/).

rhombohedral (Bi) phase is described using three unit cells (e.g. [31,32]): the standard hexagonal and primitive rhombohedral cells and a non-standard face centred rhombohedral (FCR) unit cell, which are plotted in Fig. 1(a)-(c) respectively.

Fig. 1(a) and (b) show the relationship between the triple hexagonal unit cell and primitive rhombohedral unit cell of (Bi). In Fig. 1(b), note that Bi2 (blue) is located at an off-centre position, closer to the three Bi1 atoms below (shorter orange bonds) than the three Bi1 above (longer red bonds). The non-standard FCR unit cell in Fig. 1(c) has rhombohedral angle 87.6° and highlights the pseudo-cubic nature of (Bi) and similarities to both a distorted simple-cubic structure and a distorted NaCl-type structure. Again, the Bi2 atom is not in the centre of the FCR unit cell which causes a further difference from the NaCl structure. The faces of the FCR unit cell correspond to the six $\{01\bar{1}2\}$ in the hexagonal unit cell and are the closest packed planes in bismuth. The coordination polyhedron of Bi atoms is a distorted octahedron as shown in Fig. 1(d). The tetragonal β-Sn phase also has a distorted octahedron coordination polyhedron (Fig. 1(e)) with two different bond lengths. The (Bi) crystal in Fig. 1(b)-(d) and the β-Sn crystal in Fig. 1(e) have been oriented according OR-1.

This work measures the ORs formed by eutectic solidification in Sn-58Bi solder in both controlled unidirectional solidification experiments and during solder ball solidification in an undercooled melt, and explores the factors affecting which OR, OR-variants and interfaces are selected in each case. The paper is structured in three main parts. First, we present eutectic growth twins in the (Bi) phase. Second the different eutectic ORs and growth interfaces are analysed in terms of the interplay between the twin variants and orientation variants of the ORs. Finally, we consider how the solidification conditions affect which OR is selected during eutectic growth.

2. Materials and methods

Sn-58Bi (wt%) was prepared by mixing 99.93 % Sn and 99.99 % Bi in a clay-bonded graphite crucible coated with boron nitride. This was then melted in a resistance furnace and held at 300°C for 2 hours. Subsequently, the melt was poured into a preheated silicone mould of inner dimensions 60 × 20 × 10 mm.

For unidirectional solidification experiments, the Sn-58Bi ingot was sliced into strips measuring 60 × 10 × 0.5 mm by electrical discharge machining (EDM), and then ground and cleaned in ethanol. A Sn-58Bi strip was then placed in a horizontal directional solidification apparatus with a hot zone of 190°C and a cold zone of 20.5 °C. The temperature gradient in the liquid near the solid–liquid (S–L) interface was measured to be ~ 5.32 K/mm in a separate experiment using an immersed K-type thermocouple. Samples were held stationary for 30 minutes to induce partial melting and a stable temperature gradient. Unidirectional solidification was then applied using a fixed pulling a rate in the range 0.5–40 μm/s. Near the end of growth, some samples were quenched in high pressure argon gas to enable characterisation of the quenched interface morphology.

For solidification in an undercooled melt in a differential scanning calorimeter (DSC), ~500μm diameter solder balls were used. To make the balls, first a strip of Sn-58Bi was rolled gradually to a thickness of ~0.04 mm. These sheets were then punched into 1.6 mm diameter discs and melted on a hot plate at 200℃ with a Rol-1 tacky flux to form nearly spherical balls due to surface tension. The resulting ball diameters were 500 ± 15μm. To remove residual flux, the balls were then cleaned ultrasonically in ethanol for 5 mins. Each ball was then placed in an aluminium DSC pan and melted and resolidified in a heat flux DSC (Mettler Toledo DSC1) using a cooling rate of 20 K min^{-1}.

Samples were mounted in Struers VersoCit acrylic cold mounting resin and cross-sections were prepared following standard metallographic procedures. Orientation mapping was conducted with a Bruker e-Flash electron backscatter diffraction (EBSD) detector in a Zeiss Sigma scanning electron microscope (SEM) operated at 20 kV with 13.5–15.0 mm working distance and a 70° tilted stage. Indexing was performed in Bruker ESPRIT 2.2 software using the Hough-transform method, assuming the crystal structures and lattice parameters in Table 1. Bruker ESPRIT 2.2 and Matlab with the MTEX toolbox were used to analyse the crystal orientations and interfaces. EBSD patterns were auto-indexed with the Hough transform method in Bruker ESPRIT. Additional validation of the EBSD indexing was performed for selected Kikuchi patterns using quantitative pattern matching in Bruker DynamicS as overviewed in Supplementary Information SI-Fig. 1. Since room temperature is a homologous temperature of $T/T_E \approx 72$ % for Sn-58Bi, coarsening occurs at room temperature [35] Thus, all EBSD maps were obtained within two weeks of solidification. Trials showed there were only minor changes in the eutectic microstructure in this time.

For transmission electron microscopy (TEM) of the (Bi) phase, regions with a desired orientation were first identified by EBSD orientation mapping and electron transparent samples were then made using a Ga focused ion beam (FIB) in a TFS Helios 5 CX DualBeam FIB-SEM. For TEM investigation of β-Sn + (Bi) eutectic ORs, it was found that cryogenic milling was required and electron transparent samples with a desired orientation were made using a Ga FIB in a TFS Scios-2 DualBeam FIB-SEM equipped with a cryo-stage. The temperature of the cryo-stage was set at approximately −140 °C during the initial milling and the final thinning/polishing of the TEM foils. The platinum deposition as well as the transportation of the foils to the TEM Cu grids, occurred at ambient temperature. All FIB milled samples were then investigated under a JEOL 2100 F field-emission-gun (FEG) TEM operated at 200 kV. DigitalMicrograph, SingleCrystal, and ImageJ software was used to analyse and process the TEM diffraction patterns and the HR TEM images.

3. Results and discussion

3.1. General eutectic microstructures

Typical microstructures of Sn-58Bi produced in the two solidification conditions are overviewed in Fig. 2. In both cases, the β-Sn + (Bi) eutectic had the features of a 'complex-regular' eutectic morphology comprising of local areas with a regular array of (Bi) plates, often in a fishbone structure, separated by less regular areas, consistent with prior work [19,20,23,25,36]. The samples solidified in the DSC were either fully eutectic or contained a small fraction of β-Sn dendrites depending on the undercooling as will be discussed in the final section of this paper. All unidirectionally solidified samples were fully eutectic for the growth conditions used in this paper. Note in Fig. 2(b) and (d) that the length scale of the β-Sn+ (Bi) eutectic was substantially finer in balls solidified in the DSC than in the unidirectionally solidified samples. This is related to the difference in growth undercooling in the different techniques.

Table 1
Lattice parameters and unit cells of (Bi): A7 structure with space group R-3m, and β-Sn: A5 structure with space group $I4_1/amd$. [33,34].

Phase	Unit cell	Atoms	a	B	c	α	β	γ
		per cell	[Å]	[Å]	[Å]	[°]	[°]	[°]
β-Sn	Tetragonal	4	5.835	5.835	3.182	90	90	90
(Bi)	Hexagonal	6	4.546	4.546	11.862	90	90	120
	P-rhombohedral	2	4.724	4.724	4.724	57.3	57.3	57.3
	F-rhombohedral	8	6.547	6.547	6.547	87.6	87.6	87.6

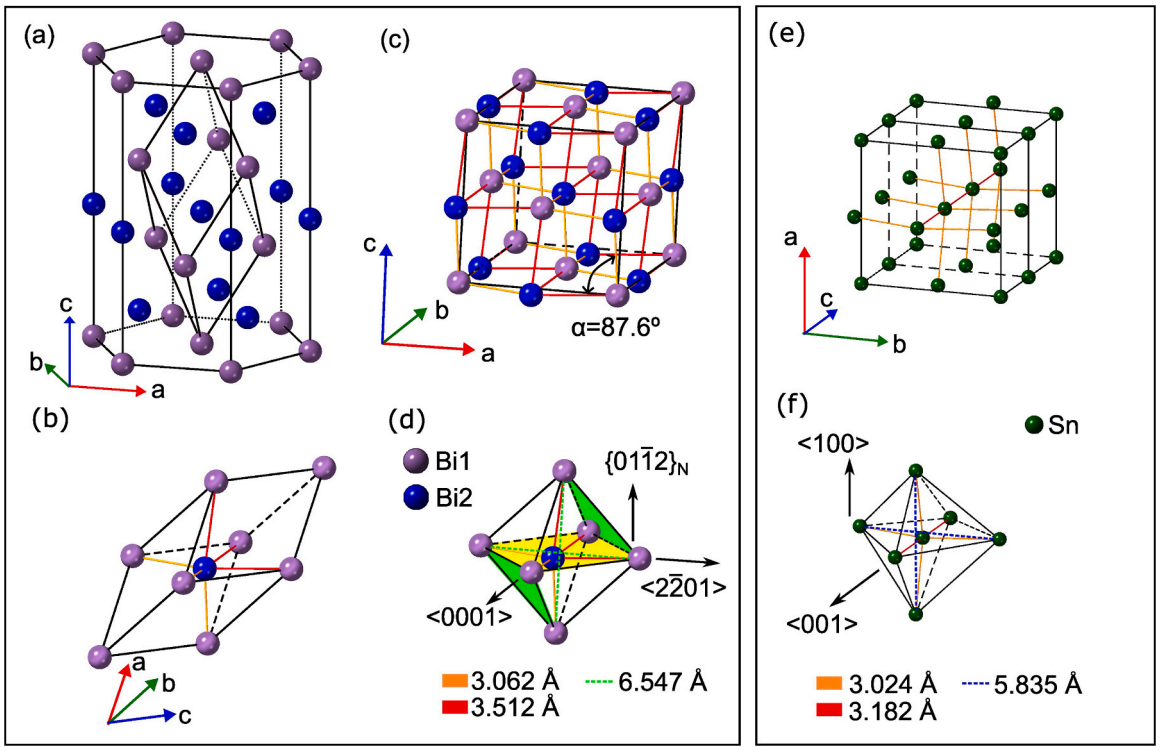


Fig. 1. (Bi) and β-Sn crystal structures. (a)-(d) various ways of viewing the (Bi) crystal structure. (a) triple hexagonal unit cell with the primitive rhombohedral unit cell indicated inside. (b) primitive rhombohedral unit cell with two bond lengths. (c) face centred rhombohedral (FCR) unit cell with pseudo-cubic NaCl-like structure and α = 87.6°. (d) distorted octahedral coordination polyhedron of (Bi). (b)-(d) have the same orientation. (e) 1x1x2 supercell of tetragonal β-Sn with two bond lengths. (f) distorted octahedral coordination polyhedron of β-Sn. (b)-(f) are oriented according to OR-1.

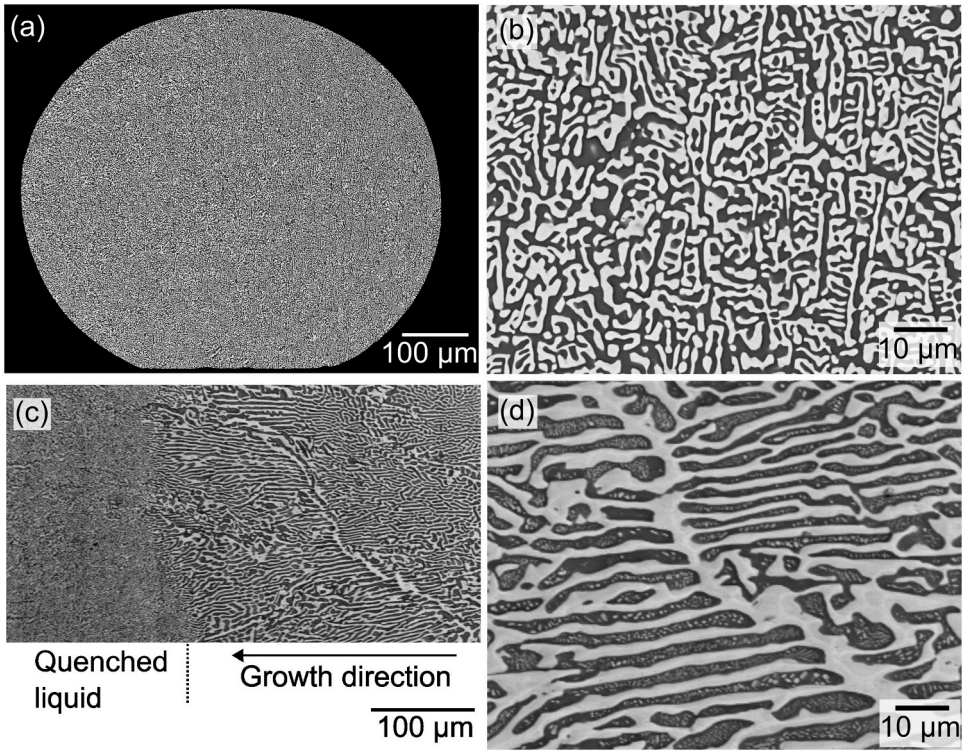


Fig. 2. BSE-SEM images of typical eutectic microstructures in Sn-58Bi. (a) and (b) ~500 μm solder ball solidified in a DSC with $\Delta T_n = 8.8$ K. (c) and (d) unidirectional solidification at a pulling rate of 5 μm/s. In (c), the sample grew from right to left and was quenched near the end of growth revealing the eutectic growth front.

Specifically, solidification in the DSC occurred after nucleation in undercooled melts of 8.8 < ΔT < 22.1 K, whereas unidirectional solidification applied pulling rates of 0.5–40 μm/s which corresponds to growth undercoolings of ≈ 0.07–0.6 K, using the growth undercooling - velocity relationship deduced previously for the Sn-Bi eutectic by Çadırlı et al. [21] of $\Delta T = (0.0093V)^{0.5}$ (in K and μm s^{-1}).

3.2. (Bi) twins in the eutectic

It was found here that eutectic (Bi) was often twinned with two twin types, one involving mirror reflection across $\{10\bar{1}4\}$ and the other across $\{01\bar{1}2\}$. These two twin types are known deformation twins in bismuth; E.g. [37–41] for $\{01\bar{1}2\} < 0\bar{1}11 >$ (which is $\{110\}<001>$ in primitive rhombohedral indices) and [42] for $\{10\bar{1}4\} < 20\bar{2}1 >$. However, here we find these twin types as growth twins in eutectic (Bi).

Fig. 3(a)-(h) shows an EBSD orientation analysis of a region of twinned eutectic (Bi). This is an unusual example where four (Bi) orientations meet at a point in eutectic (Bi) but it is a good example for demonstrating the different (Bi) twins. From the IPF-Z and IPF-Y orientation map in (b) and grain map in (c), we see that this region of eutectic (Bi) has four main orientations. EBSD patterns are shown from each orientation in Fig. 3(e), along with the unit cell orientations in Fig. 3(f) using wireframes of both the hexagonal and FCR unit cells from the measured Euler angles. Examination of the FCR unit cell orientations (light blue wireframes in Fig. 3(f)) reveals that these four (Bi) orientations are interrelated by approximately 90° rotations.

In the pole figures in Fig. 3(d), the following features can be seen: (1) all four (Bi) grains have one overlapping $\{01\bar{1}2\}$ pole and one overlapping $< 2\bar{2}01 >$ pole. (2) (Bi) grain pairs 1&2 and 3&4 have another one $< 2\bar{2}01 >$ pole and one $< 10\bar{1}1 >$ pole overlapped; And (Bi) grain pairs 1&4 and 2&3 have another one $\{01\bar{1}2\}$ pole and one $\{10\bar{1}4\}$ pole overlapped. (3) Any two of these four (Bi) grains have one $\{11\bar{2}0\} < 11\bar{2}0 >$ pole overlapped. The measured misorientation angles are 92.1° ± 0.45° for pairs 1&4 and 2&3 and 87.3 ± 0.44° for pairs 1&2 and 3&4. This can be also observed in the boundary misorientation map in Fig. 3(g) and the distribution of misorientation angles in Fig. 3(h).

These two misorientations correspond to two twin types that can be described by various angle-axis rotations as listed in Table 2 which was calculated in MTEX using the twin ORs in Fig. 3(d). In Table 2, note the following features. (i) the minimum angle-axis representation is 92.4° around $(0\bar{1}1\bar{2})_N$ for type I and 87.6° around $[\bar{2}021]$ for the type II twin. (ii) Since (Bi) has a centrosymmetric point group, a 180° rotation around a plane normal is symmetrically equivalent to mirror reflection across that plane. Thus, type I is twinning by mirror reflection across $(\bar{1}104)$ and type II is twinning by mirror reflection across $(1\bar{1}02)$. (iii) Both twin types can be obtained by rotation around a $[\bar{2}021]$ axis (180° for type I and 87.6° for type II). 1&4 and 2&3 are related by type I twinning, 1&2 and 3&4 are related by type II twinning.

Stereographic projections of the four grains in Fig. 3 are plotted in Fig. 4(a), with a small orientation change to align $< 2\bar{2}01 >$ with the viewing direction. In Fig. 4, the type I and type II twins can be generated by rotations around the common $< 2\bar{2}01 >$ axis. Moving anticlockwise from grain 1 back to grain 1 involves sequential rotations of 87.6°,

Table 2
Axis-angle representations of the two (Bi) twin types, calculated from Euler angles measured by EBSD. Entries are listed in ascending angle order.

Type I		Type II	
Axis	Angle (°)	Axis	Angle (°)
$(0\bar{1}1\bar{2})$	92.4	$[\bar{2}021]$	87.6
$(\bar{1}012)$	92.4	$[0\bar{2}2\bar{1}]$	87.6
$[04\bar{4}\bar{1}]$	117.2	$(10\bar{1}1)$	122.6
$[40\bar{4}1]$	117.2	$(01\bar{1}\bar{1})$	122.6
$(\bar{1}104)$	180	$(1\bar{1}02)$	180
$[2\bar{2}01]$	180	$[1\bar{1}0\bar{1}]$	180

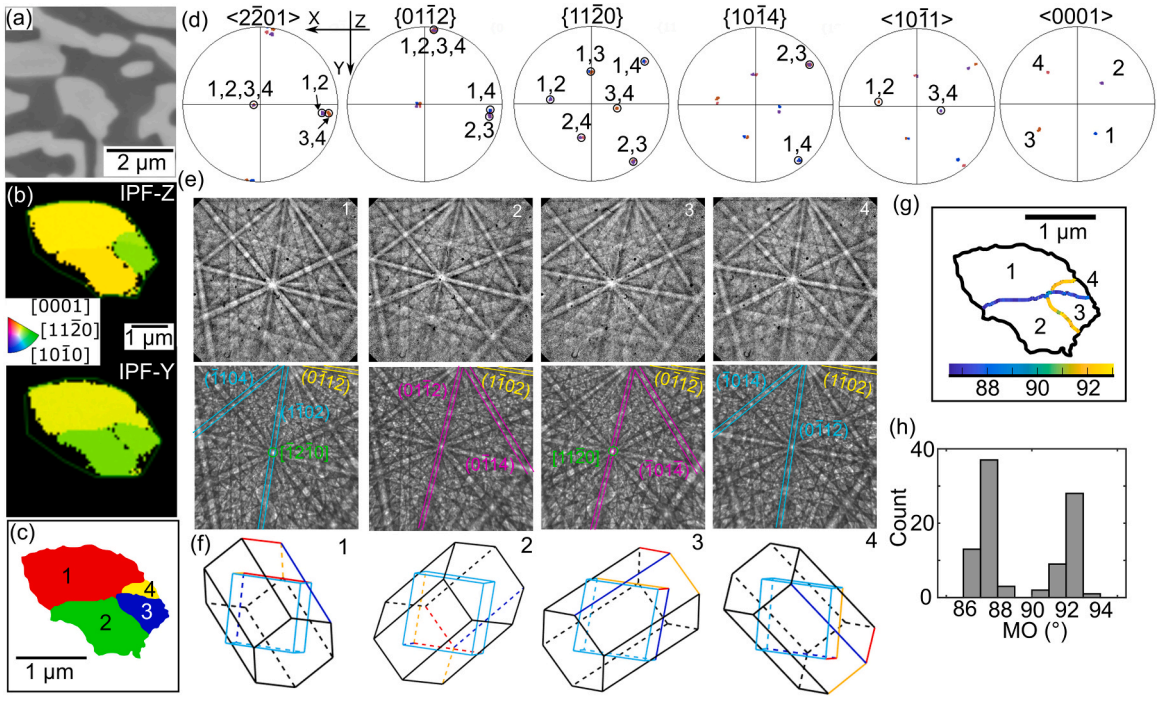


Fig. 3. EBSD analysis of eutectic (Bi) twins in a Sn-58wt% Bi solder ball solidified in a DSC with $\Delta T_n = 9.2$ K. (a) SEM-BSE image, (b) (Bi) orientation map in IPF-Z and IPF-Y colouring, (c) grain map, (d) pole figures and (e) experimental Kikuchi patterns and dynamical simulated patterns from the four main (Bi) orientations; (f) (Bi) unit cell wireframes plotted from measured Euler angles using both the hexagonal unit cell and FCR unit cell. (g) (Bi)-(Bi) boundary misorientation map with (h) the distribution of (Bi)-(Bi) misorientation angles.

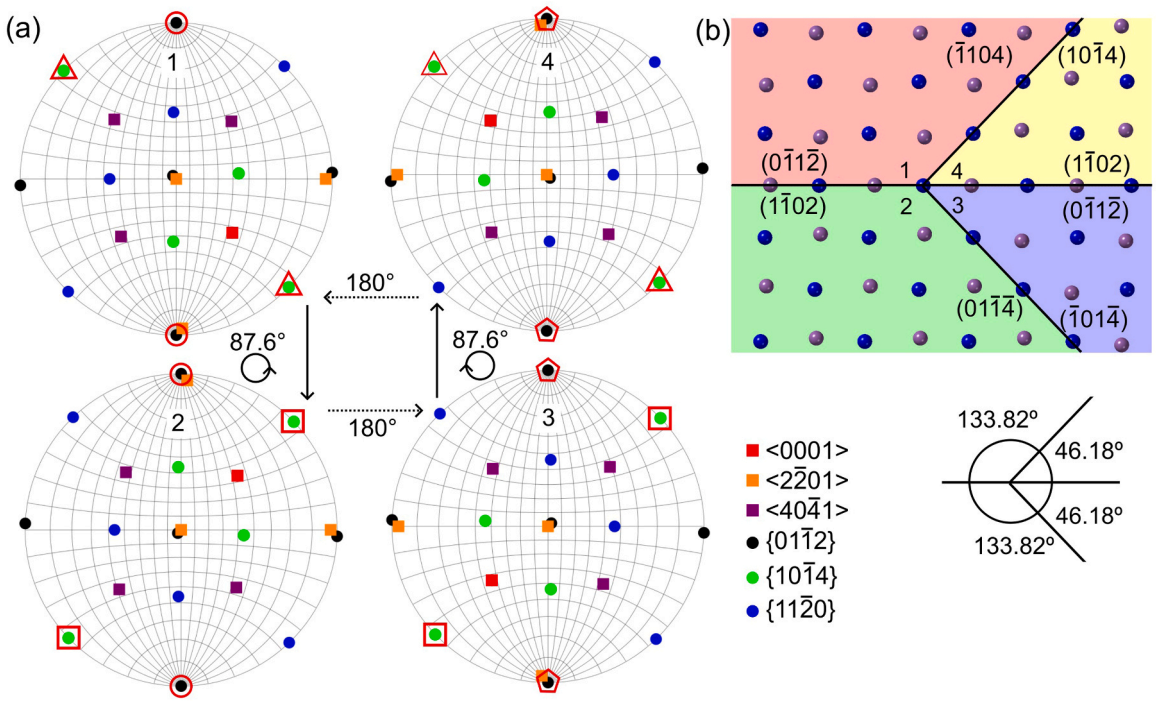


Fig. 4. Interpretation of twinned (Bi) in Fig. 3. (a) Stereographic projections of the four (Bi) orientations, slightly rotated from the pole figures in Fig. 3 to be centred on $< 2\bar{2}01 >$, with $\{01\bar{1}2\}_N$ pointing up. Open red circles, squares, pentagons and triangles mark the interface planes between orientations 1–2, 2–3, 3–4 and 4–1 respectively. The angles refer to rotation around the $< 2\bar{2}01 >$ viewing direction. (b) atomic model of the four twinned grains with the same viewing direction as (a). Note the similarity to Fig. 3(c) and (g).

180°, 87.6°, 180° around the $< 2\bar{2}01 >$ viewing direction as indicated with arrows in Fig. 4(a). The interface planes of twins are indicated with red open circles, squares, pentagons and triangles in the stereographic projections. A corresponding atomic model is shown in Fig. 4(b), also viewed along $< 2\bar{2}01 >$, which is in good agreement with the grain boundaries in Fig. 3(c).

The presence of type I and type II twins in eutectic (Bi) was confirmed by TEM as overviewed in Fig. 5. Fig. 5(a)-(c) are analysis of a $\{10\bar{1}4\}$-type twin acquired with a beam direction parallel with $< \bar{1}2\bar{1}0 >$. Fig. 5(d)-(f) are analysis of a $\{01\bar{1}2\}$-type twin acquired along $< 2\bar{2}01 >$. The selected area electron diffraction (SAED) patterns in Fig. 5(a) and (d) were taken from areas containing a pair of twinned grains and yellow circles highlight the common (overlapping) reflections. Indexing is presented on the simulated patterns in Fig. 5(b) and (e) which separate reflections from each pair of grains into red and blue, assuming a 180° rotation about the twin plane normal in both cases. HRTEM images along $< \bar{1}2\bar{1}0 >$ for twin type I and along $< 2\bar{2}01 >$ for twin type II are presented in Fig. 5(c) and (f) respectively, in which the twin interfaces are consistent with the common reflections in the SAED patterns. Note that, for the $\{01\bar{1}2\}$-type twin in Fig. 5(d)-(f), the incident beam direction is the same as the viewing direction in Fig. 4. Therefore, the HRTEM image of the $\{01\bar{1}2\}$ twin interface in Fig. 4(f) can be compared with the 1–2 and 3–4 interfaces in the atomic model in Fig. 4.

3.3. *β-Sn-(Bi) orientation relationships*

3.3.1. *Orientation relationship 1*

The two orientation relationships reported by Belyakov et al. [29] for the solid-state precipitation of (Bi) in β-Sn (written in the Introduction) were approximately measured here for β-Sn+ (Bi) eutectic growth in Sn-58Bi. However, twinned (Bi) orientations add further complexity, there are differences related to the eutectic growth morphology being different to the solid-state precipitation morphology, and some differences in the detail of the ORs were also uncovered.

A typical example of eutectic OR-1 is overviewed in Fig. 6(a)-(b) from a unidirectional solidification experiment at 5 μm/s. There is only one main β-Sn orientation and four main (Bi) orientations in this field of view. The four main (Bi) orientations can be confirmed from the four clusters in the {0001} pole figure in Fig. 6(c) that involve orange, green/blue, purple/white and white/purple IPF-X colours. The green/blue and orange (Bi) orientations occupy the majority of the area in Fig. 6(b) (80.5 %) whereas, the purple and white grains only occupy a small area fraction (19.6 %), and the sizes of the individual purple and white areas are also significantly smaller than for the green and orange (Bi) orientations. These (Bi) orientations are twinned in the same ways as the orientations in Fig. 3 and Fig. 4 although, in Fig. 6, the four (Bi) orientations are in separate regions and do not meet at one point.

While some β-Sn/(Bi) interface segments had OR-1 almost exactly such as the segment overviewed in SI-Fig. 2, most eutectic interface segments were a few degrees away from OR-1 in its strict definition. For example, in SI-Fig. 1(a), the Euler angles can be used to calculate that the phases are 2.7° from (100) ‖ $(01\bar{1}2)$ and 1.9° from [001] ‖ $[\bar{2}021]$, and inspection of the Kikuchi patterns confirms that the [001] and $[\bar{2}021]$ poles are not perfectly aligned. This is a feature of the eutectic ORs studied here; most interface segments were measured to be a few degrees of scatter away from the strict ORs. One reason for this is that twinning of (Bi) can cause a new (Bi) twin variant to deviate slightly from the β-Sn/(Bi) OR as discussed in detail towards the end of this section.

For the EBSD map in Fig. 6(a)-(b), a total of 7840 β-Sn/(Bi) interface segments were identified. Within a tolerance angle of ± 5°, 4464 out of 7840 pairs had OR-1, with an average MO angle of 54.62° ± 2.17°, compared with 54.66° for perfect OR-1, and the mean misorientation angles between the overlapping planes ({100} β-Sn // $\{01\bar{1}2\}$ (Bi)) and directions (<001 > β-Sn // $< 2\bar{2}01 >$ (Bi)) were 1.89° ± 1.05° and 2.68° ± 1.26, respectively. When the tolerance angle was increased to 10°, 7436 out of 7840 pairs satisfied the OR-1 condition, with an average

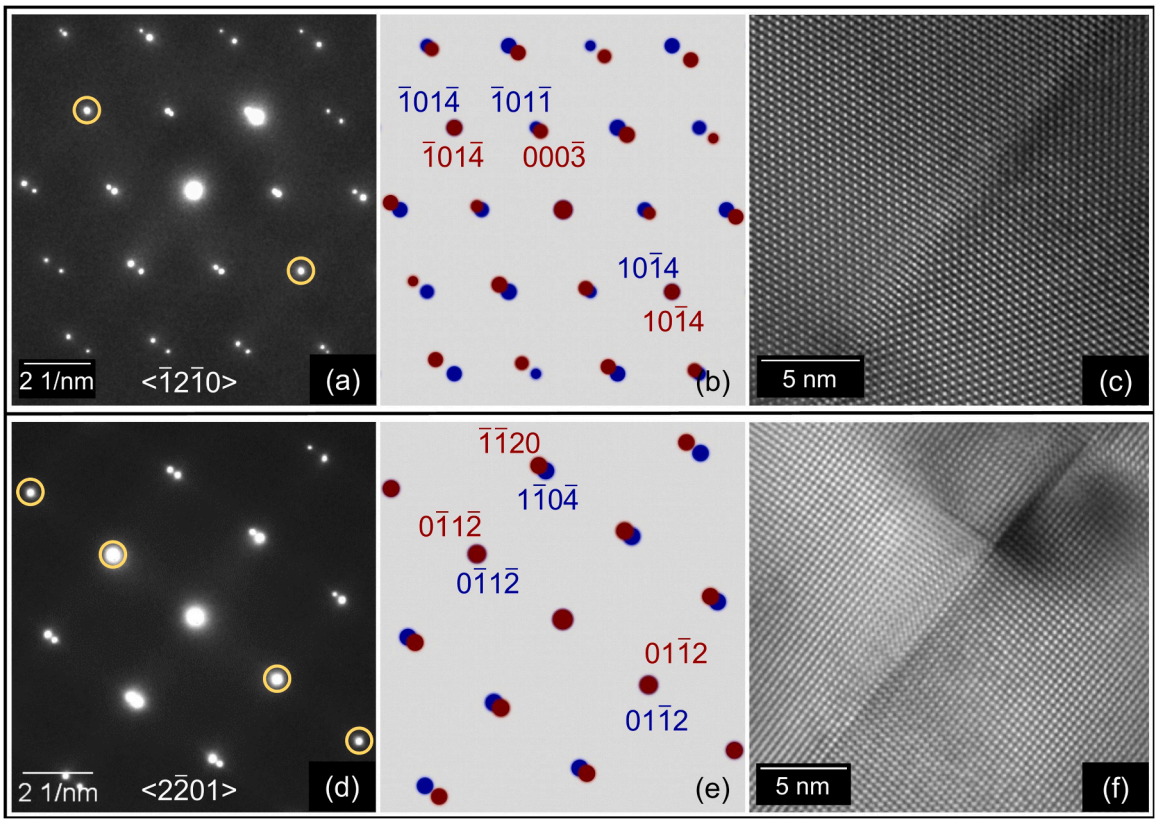


Fig. 5. TEM analysis of the two (Bi) twin types after unidirectional solidification with a pulling rate of 5 μm/s. (a) SAED pattern along $< \bar{1}2\bar{1}0 >$ from an area containing a $\{10\bar{1}4\}$ twin (type I). The yellow circles highlight the common $10\bar{1}4$ reflections. (b) Simulated SAED pattern along $< \bar{1}2\bar{1}0 >$ assuming a 180° rotation about $(10\bar{1}4)_N$. (c) HRTEM image of this type I twin along $< \bar{1}2\bar{1}0 >$. (d) SAED pattern along $< 2\bar{2}01 >$ from an area containing a $\{01\bar{1}2\}$ twin (type II). The yellow circles highlight the common $01\bar{1}2$ reflections. (e) Simulated SAED pattern along $< 2\bar{2}01 >$ assuming a 180° rotation about $(01\bar{1}2)_N$. (f) HRTEM image of this type II twin along $< 2\bar{2}01 >$.

misorientation angle of 55.74° ± 3.27°. The variation in the MO at every β-Sn/(Bi) interface segment is plotted in SI-Fig. 3 in the Supplementary Information, demonstrating how the MO varies locally around each (Bi) lamella.

Fig. 6(a)-(b) is a transverse section with growth direction in/out of the page and, thus, the (global) crystallographic growth direction is at the centre of the pole figure in Fig. 6(c). We see that the growth direction for eutectic β-Sn is $< 110 >$, which is the same as the preferred growth direction measured in prior work for β-Sn dendrites [43–47]. The corresponding growth direction of the eutectic (Bi) is $< 11\bar{2}0 >$ for the orange and green/blue (Bi) orientations and $\{10\bar{1}4\}_N$ for the purple and white (Bi) orientations. Since ~80 % of the (Bi) has orange and green/blue orientations in Fig. 6(b), it can be inferred that $< 11\bar{2}0 >$ is the preferred eutectic growth direction for (Bi). In unidirectional solidification experiments, 28 samples had regions with OR-1 and all 28 had the same (Bi) and β-Sn growth directions as Fig. 6.

Examining the pole figures in Fig. 6(c), we see that $\{01\bar{1}2\}_{(Bi)}$ and $< 2\bar{2}01 >_{(Bi)}$ have three clusters of scattered spots that overlap with the scattered spots in the pole figures of $< 001 >_{\beta\text{-Sn}}$ and $\{100\}_{\beta\text{-Sn}}$ representing OR-1, similar to [29]. However, the 87.6° angle among six $\{01\bar{1}2\}$ members in (Bi) are not equal to the 90° angle between $< 001 >$ and {100} in β-Sn. In this case, fixing a pair of parallel planes and a pair of directions as OR-1 causes a range of other planes and directions to be nearly parallel which makes the definition of OR-1 somewhat ambiguous. Analysis of misorientation angles showed that OR-1 in eutectic growth is best described as $\{100\}_{\beta-Sn} \parallel \{01\bar{1}2\}_{(Bi)}$ & $< 001 >_{\beta-Sn} \parallel < 2\bar{2}01 >_{(Bi)}$ although this results in the preferred eutectic growth directions $< 110 >_{\beta\text{-Sn}}$ and $< 11\bar{2}0 >_{(Bi)}$ being only nearly parallel. To illustrate this point, stereographic projections of OR-1 are plotted in Fig. 7 using $\{100\}_{\beta-Sn} \parallel \{01\bar{1}2\}_{(Bi)}$ and $< 001 >_{\beta-Sn} \parallel < 2\bar{2}01 >_{(Bi)}$ as indicated with black circles and squares, and using different colours and symbols to represent different plane and direction families. The misorientation angles of near-parallel planes and directions are listed in Table 3. All are ~5° or less, and the preferred eutectic growth directions $< 110 >_{\beta\text{-Sn}}$ and $< 11\bar{2}0 >_{(Bi)}$ have a misorientation of ~1.2°. Strictly, making any of the pairs in Table 3 parallel gives a different OR, but all are approximately OR-1.

Fig. 7(b)-(d) is an example of a unidirectional solidification experiment where the eutectic is growing with OR-1 and has been cross-sectioned in almost the same alignment as the stereographic projections in Fig. 7(a). This sample was quenched during growth, revealing that the eutectic growth front is serrated with facets of approximately $\{100\} \parallel \{01\bar{1}2\}$.

TEM analysis of eutectic OR-1 is overviewed in Fig. 8 from a sample unidirectionally solidified at 5 μm/s. EBSD mapping followed by cryo-FIB milling were used to produce a lamella oriented with $[001]_{\beta\text{-Sn}}$ and $[2\bar{2}01]_{(Bi)}$ parallel with the incident beam direction in TEM. From the SAED pattern taken from an area containing both phases, we see that the $(200)_{\beta\text{-Sn}}$ and $(01\bar{1}2)_{(Bi)}$ reciprocal lattice vectors are almost colinear whereas the angle between $(020)_{\beta\text{-Sn}}$ and $(\bar{1}012)_{(Bi)}$ is 2.25 ± 0.05 °. Comparing with Fig. 8 and Table 3, the TEM analysis is close to OR-1 defined as $\{100\}_{\beta-Sn} \parallel \{01\bar{1}2\}_{(Bi)}$ and $< 001 >_{\beta-Sn} \parallel < 2\bar{2}01 >_{(Bi)}$. From the HR-TEM image in Fig. 8(d), we see that the β-Sn/(Bi) interface contains relatively large steps and,

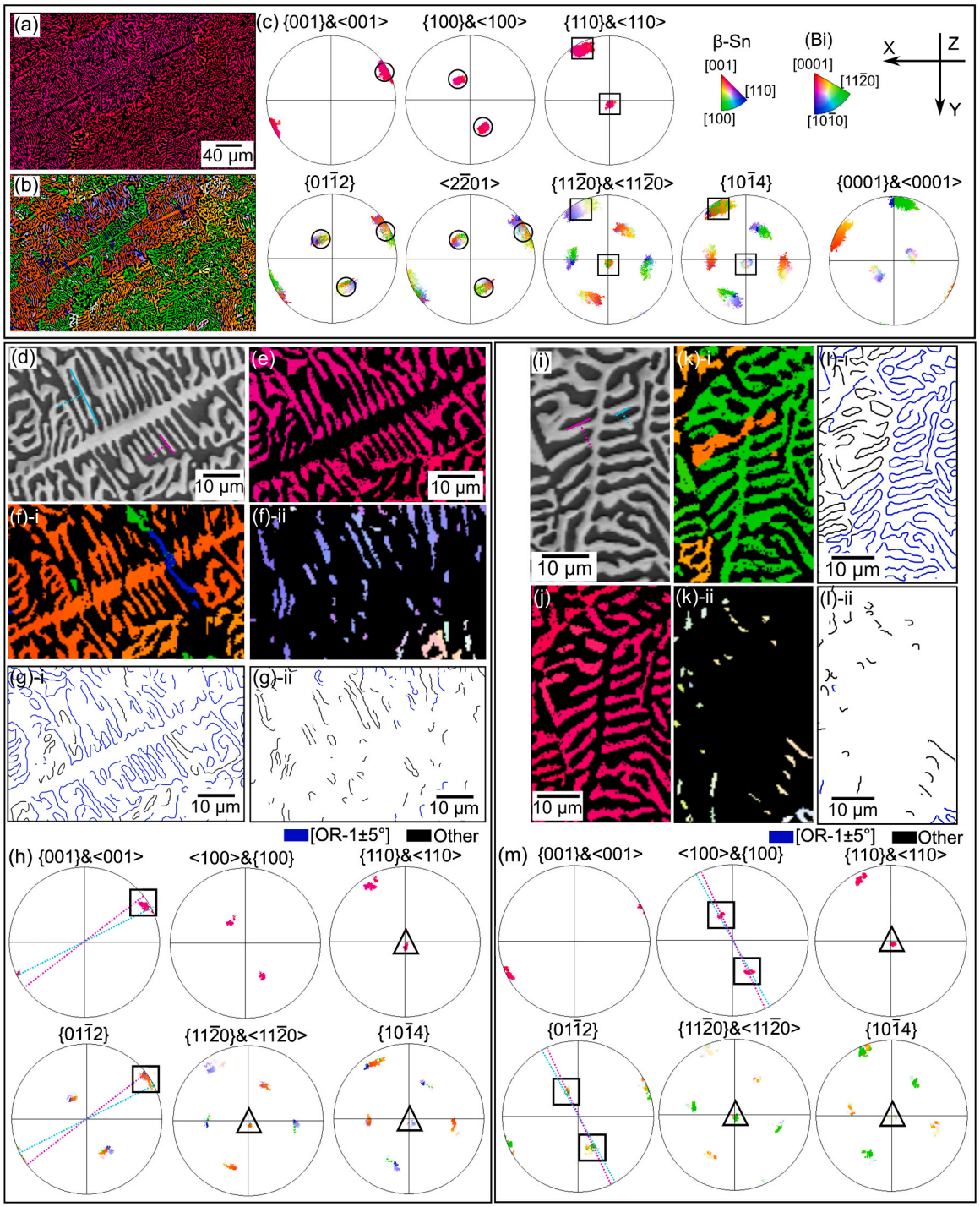


Fig. 6. Eutectic OR-1 in Sn-58wt%Bi unidirectionally solidified at 5 μm/s in transverse section (growth is out of the page). (a)-(c) wide area mapping. (d)-(h) and (i)-(m) selected areas containing fish-bone microstructure. (d), (i) are BSE-SEM images. (a), (e), (j) are EBSD orientation maps (IPF-x) of the β-Sn phase. (b), (f)-i, ii, (k)-i, ii are EBSD orientation maps (IPF-X) of the (Bi) phase, splitting the four (Bi) orientations into two groups in (f)-i, ii and (k)-i, ii based on their growth direction. (h)-(m) are selected pole figures for β-Sn (top) and (Bi) (bottom). Black squares indicate planes and directions written in OR-1. Black triangles indicate the growth direction. Coloured lines indicate the interface plane normals annotated in the same colours in the (d), (i) BSE-SEM images. (g)-i, ii and (l)-i,ii are β-Sn/(Bi) interface maps. Segments with OR-1 ± 5° are coloured blue.

combining Fig. 8(d)-(f), the long parts of the interface are $\{100\}_{\beta-Sn} \parallel \{01\bar{1}2\}_{(Bi)}$. Such stepped interfaces at the atomic and nano-scales are responsible for the curved β-Sn/(Bi) interfaces at the micro-scale (e.g. Fig. 6(d),(i) and Fig. 8(c)).

To investigate the variation in the interface planes in OR-1, two regions with fishbone microstructure in Fig. 6(a) are shown at higher magnification in Fig. 6(d) and (i) with corresponding EBSD IPF-X orientation maps for β-Sn and (Bi) in Fig. 6(e), (j), (f)-i&ii and (k)-i&ii. The EBSD orientation maps of (Bi) phase are split into two groups, i and ii, by their different direction along the heat flow direction, $< 11\bar{2}0 >$ or $\{10\bar{1}4\}_N$. Looking at the BSE images in Fig. 6(d) and (i), the eutectic β-Sn/(Bi) interfaces are often curved but are relatively straight in the more regular fishbone regions. Relatively straight interface segments have been annotated with solid cyan and pink lines in Fig. 6(d)

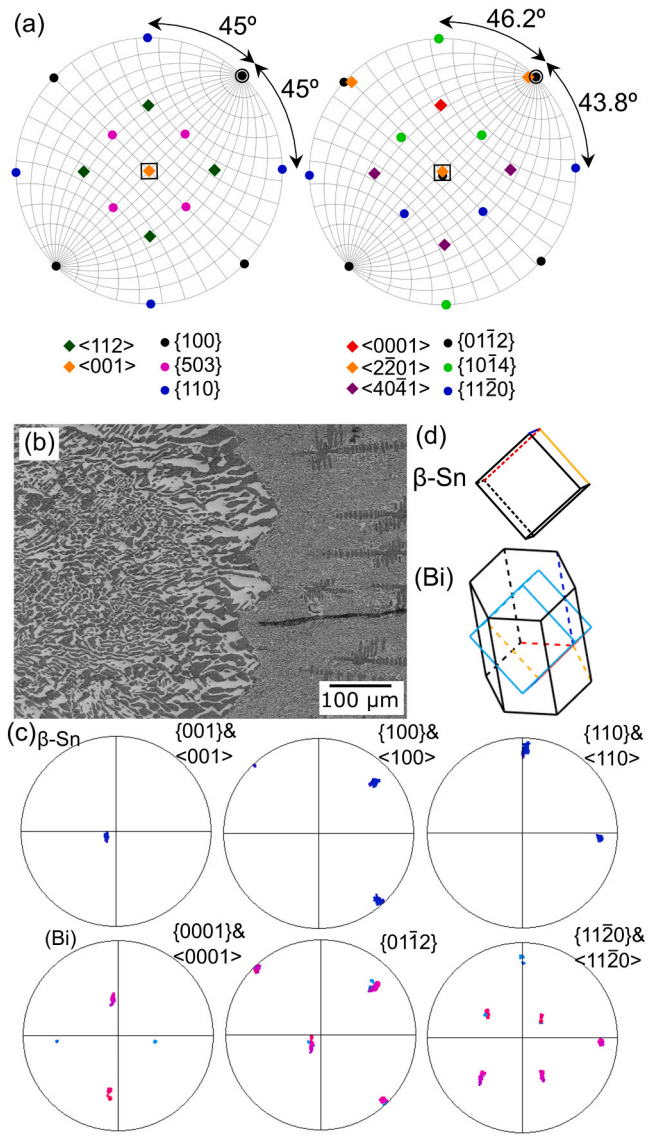


Fig. 7. Growth crystallography of unidirectional eutectic solidification with OR-1. (a) Stereographic projections of β-Sn and (Bi) with $\{100\}_{\beta-Sn} \parallel \{01\bar{1}2\}_{(Bi)}$ and $< 001 >_{\beta-Sn} \parallel < 2\bar{2}01 >_{(Bi)}$ set parallel as indicated by black circles and squares. Misorientations between nearly parallel planes and directions are listed in Table 3. (b)-(d) a sample grown at 2 μm s^{-1} that was cross-sectioned similar to (a) with growth from left to right. (b) BSE image of a quenched eutectic growth front with serrated two-phase facets. (c) Selected pole figures from EBSD showing the growth direction is approximately $< 110 >_{\beta-Sn} \parallel < 11\bar{2}0 >_{(Bi)}$ and the facets at the serrated growth front are approximately $\{100\}_{\beta-Sn} \parallel \{01\bar{1}2\}_{(Bi)}$. (c) Unit cell wireframes from the measured Euler angles. (Bi) is plotted using both the hexagonal and FCR unit cells.

and (i) and dashed lines show their projected plane normals. Dashed lines of the same colours are plotted as perpendicular bisectors on the pole figures in Fig. 6(h) and (m). For the region in Fig. 6(d)-(h), the straightest interface planes in the fishbone microstructure are consistent with $\{01\bar{1}2\}_{(Bi)}$ and $\{001\}_{\beta-Sn}$ as highlighted with black squares in the pole figures in Fig. 6(h). For the region in Fig. 6(i)-(m), the straightest interface planes are consistent with $\{01\bar{1}2\}_{(Bi)}$ and $\{100\}_{\beta-Sn}$, the same as the HR-TEM image in Fig. 8(d). These different β-Sn interface planes, {001} or {100}, result in different fishbone alignments in Fig. 6(d) and (i), and the fishbone regions in the large area in Fig. 6(a) all have one of these two alignments.

Table 3
Misorientation (MO) angles of near-parallel directions and planes in OR-1.

β-Sn	(Bi)	MO (°)
$(1\bar{1}0)/ < 1\bar{1}0 >$	$(11\bar{2}0)/ < 11\bar{2}0 >$	1.181
(110)	$(\bar{1}104)$	1.181
[112]	[0001]	1.342
$[1\bar{1}2]$	$[40\bar{4}1]$	2.081
(010)	$(\bar{1}012)$	2.464
[010]	$[\bar{2}021]$	2.464
(503)	$(10\bar{1}4)$	2.953
(001)	$(\bar{1}10\bar{2})$	3.271
$(0\bar{5}3)$	$(2\bar{1}\bar{1}0)$	3.700
$(\bar{5}03)$	$(1\bar{2}10)$	4.410
(053)	$(0\bar{1}14)$	5.090

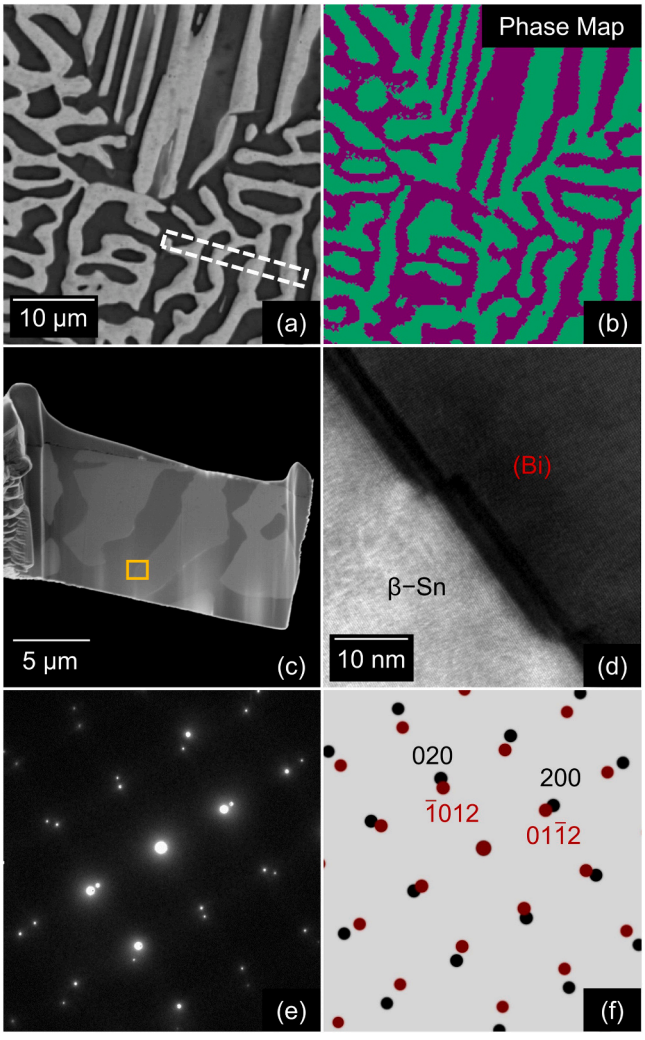


Fig. 8. TEM analysis of eutectic OR-1. (a) BSE-SEM image from Sn-58Bi unidirectionally solidified at 5 μm/s. The white dashed box indicates the location where a lamella was later extracted by cryo-FIB milling. (b) EBSD phase of map of (a). Purple=(Bi), green=β-Sn. (c) FIB lamella welded on a TEM grid. (d) TEM bright field image from the (Bi)/β-Sn interface highlighted with the yellow box in (c). (e) SAED pattern of (d). (f) Simulated SAED pattern with beam direction along $< 001 >_{\beta-Sn}$ and $< 2\bar{2}01 >_{(Bi)}$. Black = β-Sn, red = (Bi).

Note in Fig. 6(b) that both fishbone alignments sometimes had the same (Bi) orientation (e.g. green), with a single orientation of β-Sn, but $(01\bar{1}2) \parallel (001)$ and $(10\bar{1}\bar{2}) \parallel (100)$ cannot occur simultaneously and, thus, dislocations may be required to accommodate the misorientation.

At the same time, it is likely that the twinned (Bi) orientations in Fig. 6 (b) relieve interfacial strain by accommodating some of the angular difference between the (Bi) and β-Sn lattices in OR-1. For example, in the crystallographic model in Fig. 4(b), the combined four twinned (Bi) domains produce ~ 90° angles that would give angular compatibility between the (Bi) and β-Sn lattices. The resulting reduction of interfacial strain offsets the increase in interfacial area caused by growth twinning and is expected to be part of the reason why (Bi) develops growth twins during β-Sn+ (Bi) eutectic growth.

A further factor is the relationship between the (Bi) orientation variants of OR-1 and the (Bi) twin variants of twin types I and II. As overviewed in Fig. 9 and its caption, for a single orientation of β-Sn, there are eight different ways that (Bi) can be oriented with OR-1 and these eight (Bi) OR-1 variants are similar to the (Bi) twin variants generated by twin types I and II. In Fig. 9(b)-(d), note that the (Bi) unit cell wireframes are arranged in a 4 × 4 matrix where each column contains similar (but not the same, in most cases) orientations. While there are approximately four (Bi) orientations, more precisely the calculations give four groups each containing multiple slightly different orientations depending on whether a (Bi) orientation is an OR-1 variant,

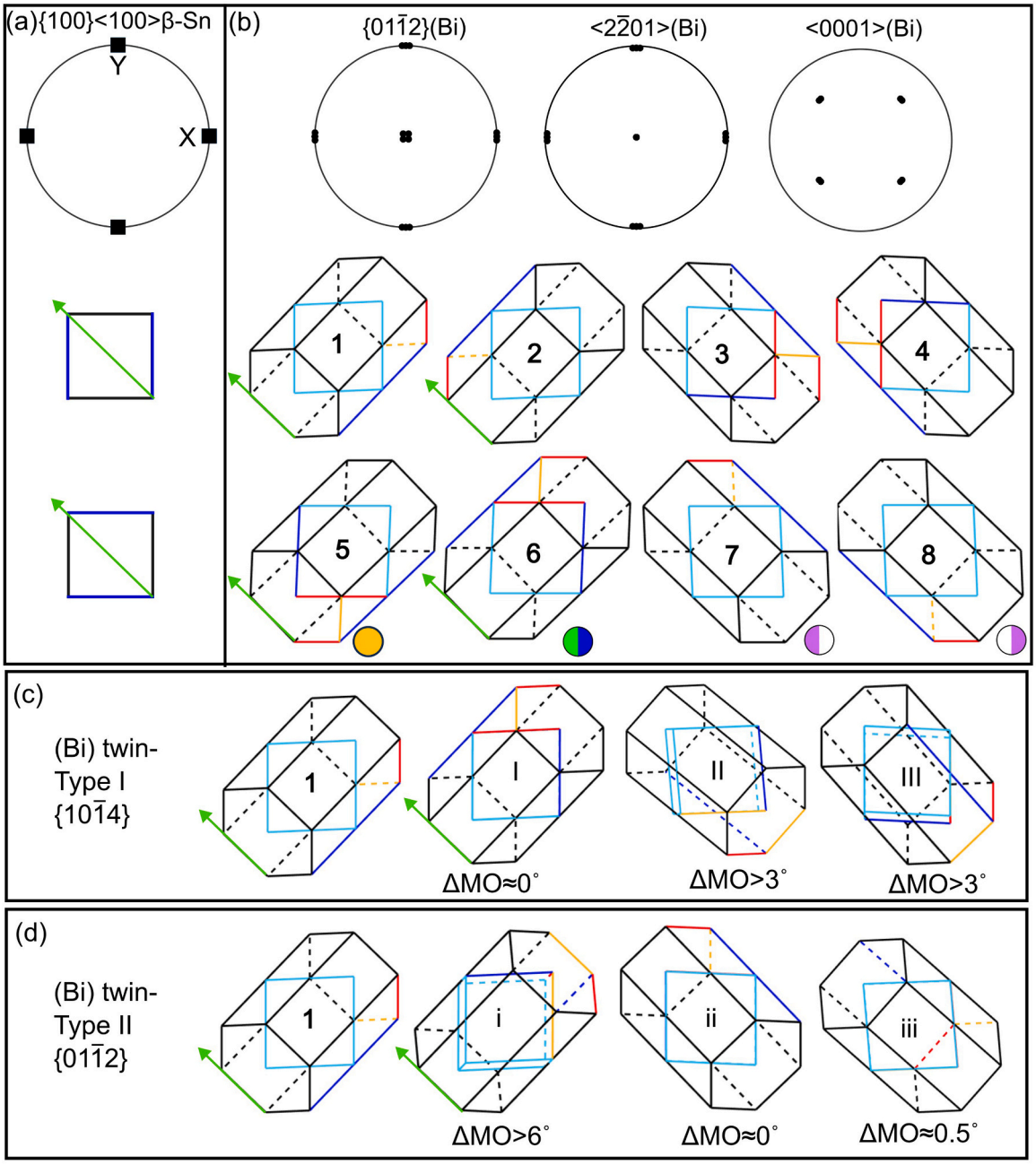


Fig. 9. Similarities among the OR-1 variants and twin variants of (Bi), demonstrated using pole figures and unit cell wireframes calculated in MATLAB with the MTEX toolbox. (Bi) is plotted using both hexagonal and FCR unit cells. (a)-(b) For a single orientation of β-Sn, there are eight orientation variants of (Bi) with OR-1. In the middle row of (b), $(100)_{\beta\text{-Sn}}$ is parallel with various $\{01\bar{1}2\}_{(Bi)}$. In the bottom row of (b), $(010)_{\beta\text{-Sn}}$ is parallel with various $\{01\bar{1}2\}_{(Bi)}$. (c) are the twin variants of the $\{10\bar{1}4\}_{(Bi)}$ twin (type-I) applied to (Bi) orientation 1. (d) are the twin variants of the $\{01\bar{1}2\}_{(Bi)}$ twin (type-II) applied to (Bi) orientation 1. ΔMO values are the difference between the MO to β-Sn in OR-1 (54.66 °) and the MO to β-Sn for each (Bi) twin variant. Green vectors are the growth direction in unidirectional solidification: $<110>_{\beta-Sn} \| <11\bar{2}0>_{(Bi)}$. The four coloured discs at the bottom of (b) correspond to the four main orientations (colours) in the {0001} pole figure in Fig. 6(c).

a type-I twin variant, or a type-II twin variant.

The calculations in Fig. 9 can be linked to the experimental results in Fig. 6. Choosing the green vector in Fig. 9(b)-(d) to be the specific $<110>_{\beta-Sn} \| <11\bar{2}0>_{(Bi)}$ growth direction in eutectic solidification, we can assign the four main orientations in Fig. 6 to the four columns in Fig. 9(b)-(d)) using orange, green/blue, purple/white and white/purple from the IPF-X colouring of Fig. 6(c) (the four colour groups are most easily seen in the {0001} of Fig. 6(c)). To investigate which orientation variants were selected in eutectic growth, the large region in Fig. 6(a) and (b) was further analysed as overviewed in Fig. 10. The (Bi) twin type is presented in Fig. 10 (b) and the OR type in (c), along with two histograms showing the distribution of misorientation angle between (Bi)/(Bi) in (d) and β-Sn/(Bi) in (e). In Fig. 10 (b), type I twins (90–95°, coloured green) account for 70.5 % of the total (Bi)/(Bi) boundary length, while type II twins (85–90°, coloured red) account for 10.2 %. This is further shown in the (Bi)-(Bi) MO histogram in Fig. 10 (d) where there is clear separation between the two twin peaks, and the 92.4° type I twin peak is much larger than the 87.6° type II twin peak. Thus, across this large region, there is a strong preference for $\{10\bar{1}4\}_{(Bi)}$ twins (type I) and there are two dominant (Bi) orientations, orange and green/blue in Fig. 6(b)) that both have $<110>_{\beta-Sn} \| <11\bar{2}0>_{(Bi)}$ in the eutectic growth direction Fig. 6(c). Comparing this with Fig. 9(c) and (d), note that only $\{10\bar{1}4\}_{(Bi)}$ twins (type-I) have a twin variant that simultaneously maintains $<110>_{\beta-Sn} \| <11\bar{2}0>_{(Bi)}$ in the eutectic growth direction and maintains OR-1 between the β-Sn and the two twinned (Bi) orientations (i.e. has a near-zero ΔMO). This is likely to be the origin of the preference for $\{10\bar{1}4\}_{(Bi)}$ growth twins (type-I) in Fig. 10 (b) and (d) and the selection of two main (orange and green/blue) (Bi) orientations in Fig. 6(b).

Considering the specific pair of orientations across each (Bi)-(Bi) twin segment in Fig. 10 (b) revealed that, while twins between the orange and green/blue (Bi) orientations had 73 % of the boundary length with twin type I as discussed in the previous paragraph, twins involving orange or green/blue orientations and the minority white/purple orientations, had 55 % of their twin boundary length with twin type II. Consistent with this preference, note in Fig. 9(c) and (d) that $\{01\bar{1}2\}_{(Bi)}$ twins (type-II) between orientation 1 and ii or iii have lower ΔMO value than $\{10\bar{1}4\}_{(Bi)}$ twins (type-I) between orientation 1 and II or III.

Next, consider the phase boundary map indicating eutectic orientation relationships in Fig. 10 (c). OR-1 ± 5° (blue) occupies most of the area and there are also black boundary segments corresponding to 'other' OR. Examination of the MO histogram in Fig. 10 (e) shows a single wide peak centred near the theoretical MO for OR-1 (54.66 °). We see that the peak is wider than ± 5° and, therefore, the black boundary segments in Fig. 10 (c) are more than 5° away but are still related to OR-1. This orientation scatter is partly due to some twin variants having a ΔMO > 3° in Fig. 9(c) and (d). This can be seen in more detail in the analysis of a small region at higher magnification in Fig. 6(g) and (l). In the β-Sn/(Bi) interface maps shown in Fig. 6(g)-i, (g)-ii, (I)-i, and (I)-ii corresponding to (f)-i, (f)-ii, (k)-i, and (k)-ii, blue lines are interface segments with OR-1 within a tolerance of ± 5° and black lines are interface segments outside this tolerance limit. The maps are split into two groups, i and ii, by their different direction along the heat flow direction, $<11\bar{2}0>$ or $\{10\bar{1}4\}_N$. (Bi) orientations with $<11\bar{2}0>$ in the growth direction have 84 % of their β-Sn/(Bi) interface length with OR-1 ± 5°, whereas (Bi) with $\{10\bar{1}4\}_N$ in the growth direction have only 30 % with OR-1 ± 5°. Noting that most (Bi) twins in Fig. 6(g) and (l) are type I twins, this result is consistent with the calculations in Fig. 9(c) and (d), i.e. the twin variants that maintain $<11\bar{2}0>$ in the growth direction (1 and I in Fig. 9(c)) have ΔMO ≈ 0 and, therefore, maintain OR-1 with β-Sn. The twin variants that do not have $<11\bar{2}0>$ in the growth direction (II and III in Fig. 9(c)) have ΔMO > 3° and, therefore, are somewhat away from OR-1 with β-Sn.

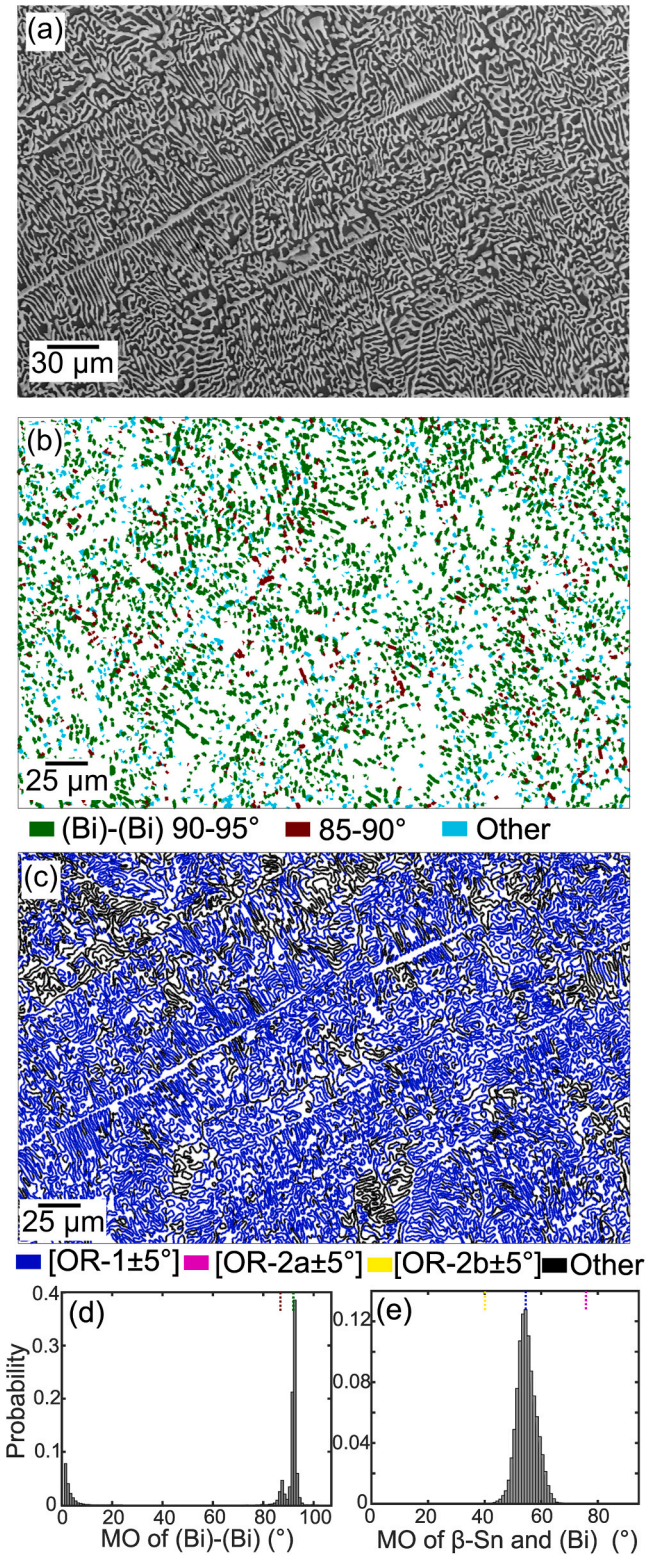


Fig. 10. Relationship between OR-1 and (Bi) twin types in the large area in Fig. 6(a)-(b). (a) BSE image; (b) (Bi)-(Bi) twin boundary map. Type I $\{10\bar{1}4\}$ twins defined with MO = 90–95°are coloured green. Type II $\{01\bar{1}2\}_{(Bi)}$ twins with MO = 85–90°are coloured red. (c) phase boundaries coloured by eutectic orientation relationship using a ± 5° threshold. (d) histogram of MO angles at (Bi)/(Bi) boundaries. Short green and red lines from the top axis indicate the theoretical MO for type I and type II twins respectively. (e) histogram of MO angles between β-Sn and (Bi). Short blue, pink and yellow lines from the top axis indicate the theoretical MO for OR-1, OR-2a, and OR-2b of 54.66°, 77.92° and 40.82° respectively.

In summary, in eutectic growth with OR-1, the dominant (Bi) twin variants are those which simultaneously have $< 11\bar{2}0 >$ in the growth direction and OR-1 with the surrounding β-Sn. However, the other twin variants also exist as minority orientations and tend to deviate from OR-1 by a few degrees.

The (Bi) orientation maps in Fig. 6 also reveal a (Bi) twin microstructure that spans multiple length scales from the macro twin domains visible in Fig. 6(b) to the individual twinned (Bi) lamellae in Fig. 6(f)-i and (k)-i. Specifically, there were large domains of mostly one twin variant spanning tens of lamellar widths and, within each domain, some individual (Bi) lamellae had a different twin variant. For example, the blue (Bi) lamella in a mostly orange (Bi) domain in Fig. 6(f)-i, and the orange (Bi) lamella in a mostly green (Bi) domain in Fig. 6(k)-i. This lamellar length scale depends on the solidification conditions, and the quantitative relationship between lamellar spacing, growth velocity and undercooling for the Sn-Bi eutectic has been reported elsewhere [21]. Further work is required to determine if the macro-domains and the multi scale twin microstructure also varies systematically with solidification conditions such as growth velocity. To gain a deeper understanding of the 3D microstructure and interfaces, future research could also consider 3D EBSD and diffraction contrast tomography (DCT) techniques.

3.3.2. OR-2 and a comparison of the ORs

OR-2 was reported for solid-state (Bi) precipitation by Belyakov et al. [29] to be $\{100\}_{\beta-Sn} \parallel \{01\bar{1}2\}_{(Bi)}$ and $< 011 >_{\beta-Sn} \parallel < 2\bar{2}01 >_{(Bi)}$. We find that OR-2 is more precisely two ORs that we name OR-2a and OR-2b. This can be seen in the EBSD analysis of Sn-Bi eutectic growth in Fig. 11 from unidirectional solidification at a pulling rate of 2 μm/s. The ORs are shown using the pole figures in Fig. 11 (c)-(e), with the near-parallel planes and directions indicated by black circles and squares. (Bi) regions with OR-2a and OR-2b are separated in Fig. 11 (d)-(e) where they can be distinguished in the pole figures by different planes in (Bi) aligning nearly parallel to {012} in β-Sn, specifically $\{11\bar{2}0\}$ in OR-2a and $\{10\bar{1}4\}$ in OR-2b as indicated by the black triangles. Applying a tolerance limit of 5°, a β-Sn/(Bi) interface map is plotted in Fig. 11 (b) revealing that most phase boundary segments have either OR-2a or OR-2b in this region. These two ORs can be distinguished by writing them as:

$\{101\}_{\beta-Sn} \parallel \{01\bar{1}2\}_{(Bi)}$ and $< 010 >_{\beta-Sn} \parallel < 2\bar{2}01 >_{(Bi)}$ OR-2a

$\{101\}_{\beta-Sn} \parallel \{10\bar{1}2\}_{(Bi)}$ and $< 010 >_{\beta-Sn} \parallel < 2\bar{2}01 >_{(Bi)}$ OR-2b

Note that while these (Bi) planes and directions are from the same families, they result in different ORs because they cause inequivalent plane families in (Bi) to be parallel to one plane family in β-Sn. For example, $\{11\bar{2}0\}$ is near-parallel with {012} in OR-2a while $\{10\bar{1}4\}$ is near-parallel with {012} in OR-2b. This is related to the relatively small rhombohedral distortion of (Bi), α = 87.6 ° in the FCR unit cell in Fig. 1 (c) and Table 1, where $\{11\bar{2}0\}$ and $\{10\bar{1}4\}$ correspond to {110} and $\{1\bar{1}0\}$ respectively in FCR indices which would both belong to one plane family if there was no rhombohedral distortion, i.e. if (Bi) was simple cubic in Fig. 1(c). Fig. 12 (a) visualises OR-2a and OR-2b using unit cells and compares them with OR-1. The ORs can be distinguished by an $\{01\bar{1}2\}_{(Bi)}$ being parallel to $\{101\}_{\beta-Sn}$ in OR-2a and OR-2b, whereas $\{01\bar{1}2\}_{(Bi)}$ is only parallel to $\{100\}_{\beta-Sn}$ in OR-1. The ORs can also be distinguished by the rotation angle between β-Sn and (Bi). The misorientation (MO) = 54.66° in OR-1, MO = 77.92° in OR-2a and MO = 40.82° in OR-2b for the lattice parameters in Table 1.

In the more regular eutectic regions, the main β-Sn/(Bi) interface planes were the same in OR-2a and OR-2b as overviewed in Fig. 11. From the BSE image in Fig. 11 (a), we see that eutectic growth with OR-2a and OR-2b both involved one main interface alignment as marked by the annotated dashed green line which marks the projection of this interface plane normal in the cross-section. A similar dashed green line is plotted as a perpendicular bisector in the pole figures in Fig. 11 (c)-(e), demonstrating that the main interface is consistent with {101} of β-Sn and $\{01\bar{1}2\}$ of (Bi) for both OR-2a and OR-2b. $\{101\}_{\beta-Sn} \parallel \{01\bar{1}2\}_{(Bi)}$ is a logical interface plane for OR-2a and OR-2b since it has a much lower planar atomic disregistry compared to other near-parallel planes in OR-2a and OR-2b, including $\{100\}_{\beta-Sn} \parallel \{01\bar{1}2\}_{(Bi)}$ with $< 011 >_{\beta-Sn} \parallel < 2\bar{2}01 >_{(Bi)}$, using a Bramfitt approach [48,49] as shown in Table 4.

For all the orientation relationships, OR-1, OR-2a and OR-2b, the $\{01\bar{1}2\}$ of (Bi) forms the largest interface with β-Sn in regions with a locally regular eutectic microstructure. $\{01\bar{1}2\}$ in hexagonal indices corresponds to the {100} faces of the FCR unit cell in Fig. 1(c) and are the closest packed planes in (Bi). For the β-Sn phase, the main interface is {100} in OR-1 and {101} in OR-2a and OR-2b. We note that other studies on solidification ORs involving β-Sn also report multiple ORs, where $\{100\}_{\beta-Sn}$ in one OR and $\{101\}_{\beta-Sn}$ in another OR are both parallel to one plane in the other phase. For example, this is reported in ORs between β-Sn and $NiSn_4$ [50], Ti_2Sn_3 [51], and Ag_3Sn [52] and is the

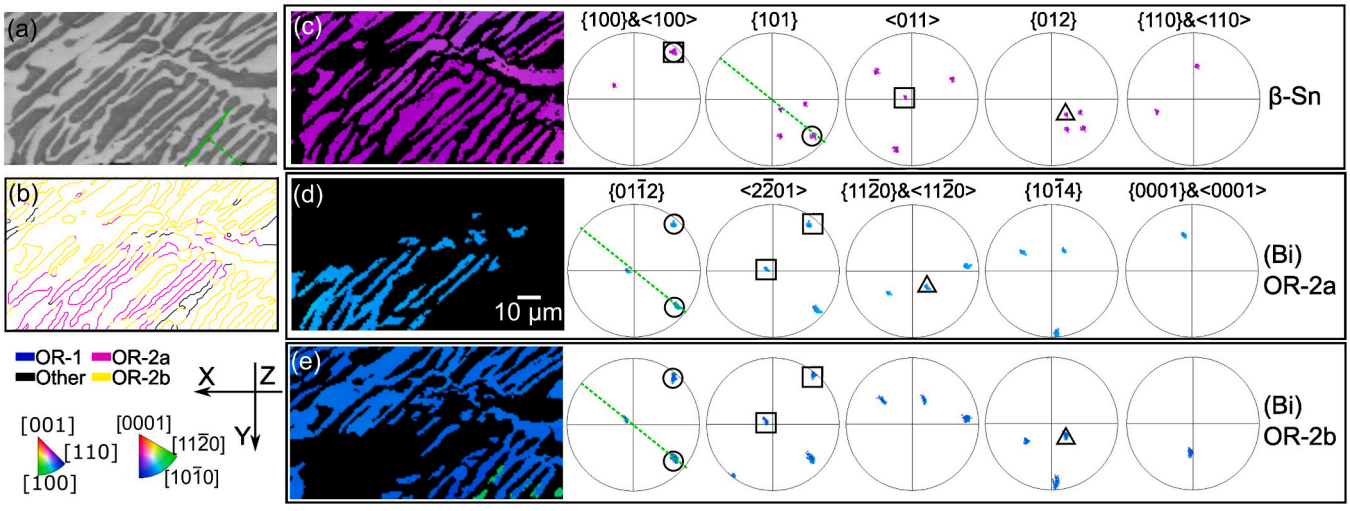


Fig. 11. Eutectic OR-2 in Sn-58wt%Bi unidirectionally solidified at 2 μm/s in longitudinal section (growth is from right to left). (a) BSE-SEM image. (b) β-Sn/(Bi) interface map showing segments within ± 5° of each OR. (c) EBSD orientation map (IPF-Z) of the β-Sn phase. (d) and (e) EBSD orientation maps (IPF-Z) of the (Bi) phase, splitting the four (Bi) orientations into two groups based on their different planes near-overlapping with {012} in β-Sn. Black circles and squares in the pole figures indicate parallel planes and directions in OR-2. Black triangles in the pole figures are to distinguish OR-2a and OR-2b.

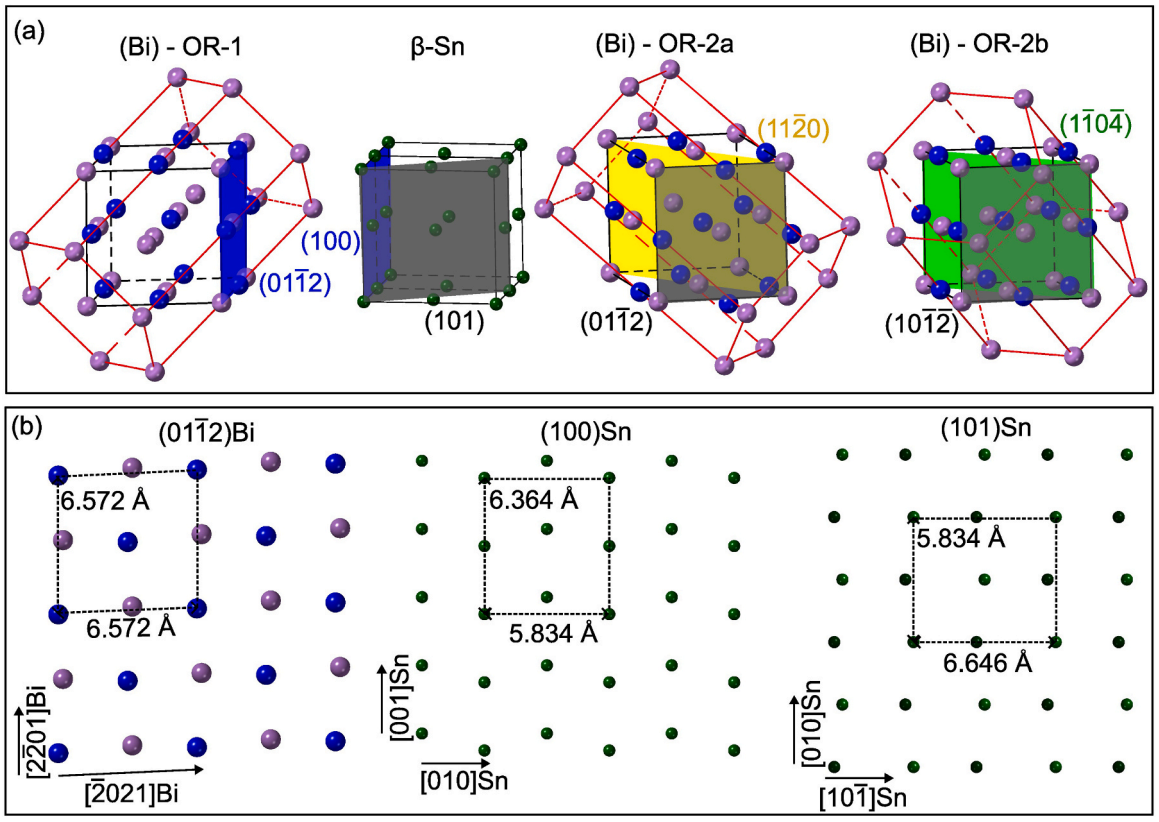


Fig. 12. Atomic models of the eutectic ORs. (a) (Bi) and β-Sn unit cells oriented according to OR-1, OR-2a and OR-2b. (Bi) is plotted with both hexagonal (red) and FCR (black) unit cells. Blue {01$\bar{1}$2} ‖ {100} planes are the main interface planes in OR-1. Grey {01$\bar{1}$2} ‖ {101} planes are the main interface planes in OR-2a and OR-2b. Note that the yellow {11$\bar{2}$0}-type (Bi) plane in OR-2a is near-parallel with the green {10$\bar{1}$4}-type Bi plane in OR-2b. These correspond to {110} and {1$\bar{1}$0} of (Bi) in FCR indices. (b) Atoms in the {01$\bar{1}$2}-type interface planes of (Bi) compared with {100} and {101} of β-Sn.

Table 4
Atomic matching across the interface for OR-1 and OR-2 summarizing the planar disregistry using Bramfitt method. Further details are in SI-Fig. 4.

	(1$\bar{1}$02)[$\bar{2}$021]	($\bar{1}$012)[2$\bar{2}$01]	(01$\bar{1}$2)[$\bar{2}$021]
OR−1	(001)[010] 10.7 %	(100)[001] 6.6 %	(010)[001] 6.6 %
OR−2	(301)[010] 12.5 %	(101)[010] 5.2 %	(010) [10$\bar{1}$] 14.4 %

case for (Bi) in Fig. 12 (a). This repeated result seems to be due to the relative similarity in the atomic positions in the {100} and {101} of β-Sn as can be seen in Fig. 12 (b). Examining Table 4, note that {101} in OR-2 has a slightly better atomic match to {01$\bar{1}$2} of (Bi) than {100} does in OR-1. However, OR-2 has worse atomic matching to the other {01$\bar{1}$2} planes in (Bi) which form as the minor interfaces.

3.4. Competition between the eutectic ORs

In unidirectional solidification experiments, all three eutectic ORs were typically present near the start of growth and OR-1 then became the dominant OR during competitive growth. For example, Fig. 13 overviews EBSD analysis of a sample where the pulling rate was 0.5 μm/s and growth was from left to right. Fig. 13 (a)-(d) includes three regions at different growth distances from the start of growth. The left region spans from 0 – 1.9 mm of growth, the middle region from 4.4 – 4.8 mm and the right region spans from 35.2 – 36.5 mm of steady-state growth. The boundary segments between the two phases have been coloured blue, pink and yellow for OR-1, OR-2a and OR-2b respectively in Fig. 13 (d). Here a tolerance limit of 10 degrees was set for each OR. In Fig. 13 (d), we see that OR-1, OR-2a and OR-2b were all present at the start of growth (0 mm) and that OR-1 gradually became dominant during growth. The pie charts in Fig. 13 (e) quantify the proportions of OR-1, OR-2a and OR-2b phase boundary length in the five regions (i-v), indicated by white vertical dashed lines in Fig. 13 (c). OR-1 increases from 34 % near the start of growth to 88 % during steady-state growth in region v, and the proportions of OR-2a and OR-2b fall to essentially zero.

Note in the EBSD IPF-X maps in Fig. 13 (b) and (c), that multiple grain orientations are present near the start of growth and competitive growth resulted in a dark blue β-Sn grain being selected (Fig. 13 (b)) where dark blue corresponds to $< 110 >$ in the growth direction (X), similar to in Fig. 6. The multiple (Bi) orientations towards the end of growth in Fig. 13 (c) are the four main twinned (Bi) orientations with OR-1 to the main β-Sn orientation presented earlier.

14 unidirectional solidification samples were investigated, with pulling rates from 0.5 to 40 μm/s. In 13 samples, OR-1 prevailed over OR-2, becoming the dominant eutectic orientation relationship in steady-state growth. In the one exception, OR-2 overgrew OR-1 early during growth such that OR-1 was absent and not part of competitive growth by the time that steady state was reached.

The preference for OR-1 during unidirectional solidification seems to arise because it allows all {01$\bar{1}$2} of (Bi) to have a reasonable atomic match to the {100} and {001} of β-Sn which does not occur between {01$\bar{1}$2} of (Bi) and all relevant planes of β-Sn in OR-2 (Table 4). Additionally, OR-1 allows the preferred growth direction of each phase, $< 110 >_{\beta\text{-Sn}}$ and $< 11\bar{2}0 >_{(Bi)}$, to be simultaneously parallel with the heat flow direction. Thus, OR-1 offers a lower total interfacial energy and a growth advantage over OR-2 during unidirectional growth.

A similar analysis was applied to 32 Sn-58Bi solder balls that solidified in the DSC with different undercoolings. An example of a DSC thermogram defining the melt undercooling, ΔT_n, is given in Fig. 14 (b). Fig. 14 (a) plots the phase boundary segments according to their OR in

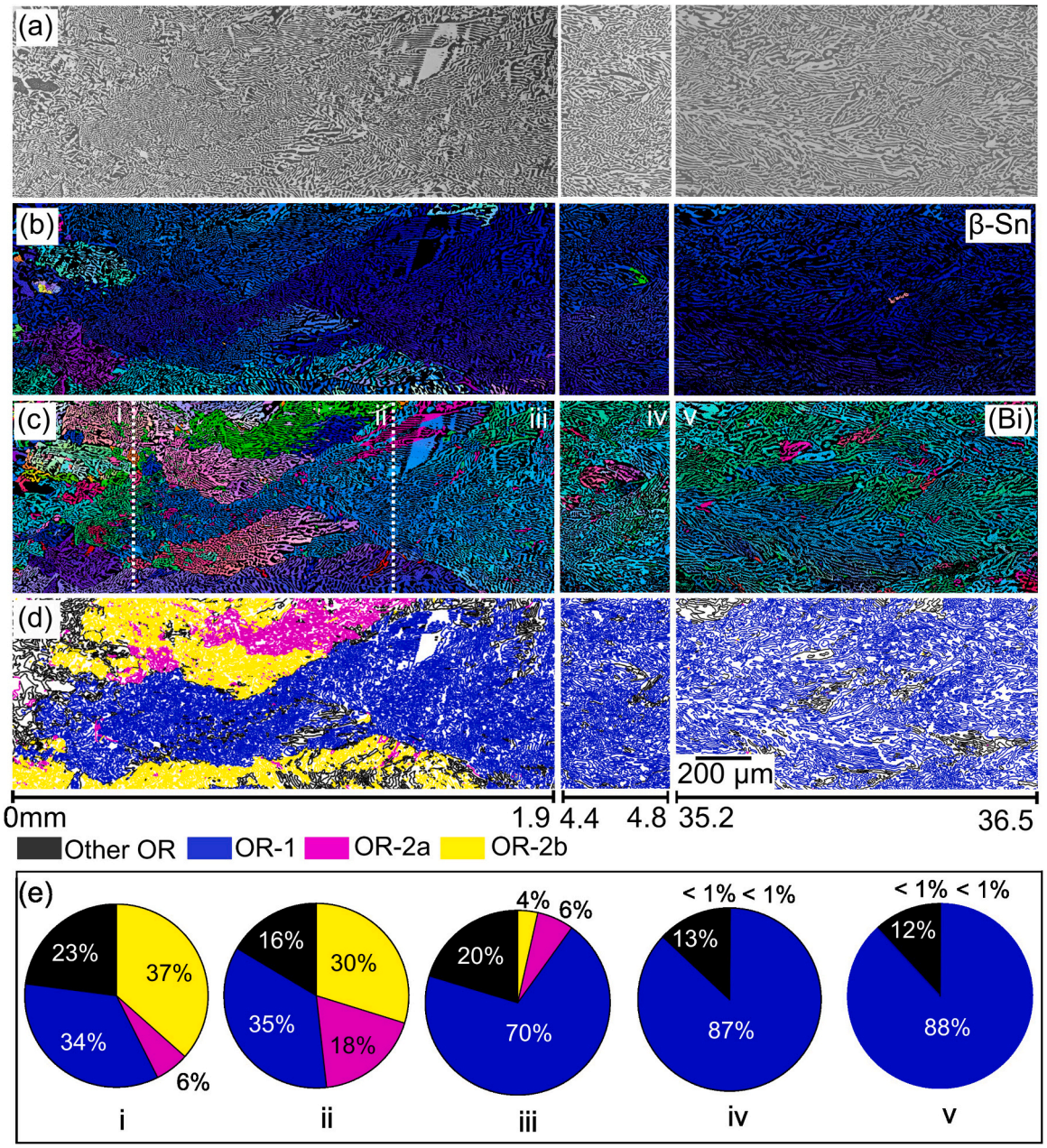


Fig. 13. Competition between eutectic ORs during unidirectional solidification at 0.5 μm/s. (a) BSE images; (b) β-Sn orientation maps (EBSD IPF-X); (c) (Bi) orientation maps (EBSD IPF-X); (d) phase boundaries coloured by eutectic orientation relationship: blue = OR-1, pink = OR-2a, yellow = OR-2b. Longitudinal section with growth direction to the right. Growth started near the left side of the leftmost image/map.

five solder balls that solidified at different melt undercoolings. Note that Fig. 14 (a) is arranged by undercooling, with the ball with smallest undercooling at the top and deepest undercooling at the bottom. It is evident in these five examples that, at the smallest undercooling, the eutectic OR was predominantly OR-1 and, as the melt undercooling became deeper, the proportion of the eutectic microstructure with OR-2 increased. To present statistically significant results, the phase boundary length fractions of the ORs in the EBSD maps of 32 solder balls are combined in a stacked column chart in Fig. 14(d), separated into bins of different melt undercooling. This confirms the increasing proportion of OR-2 and decreasing proportion of OR-1 as the melt undercooling became deeper. We also see in Fig. 14 (b) that the ratio between OR-2a and OR-2b is broadly similar in each bin, indicating that the 'a' and 'b' versions of OR-2 exhibited no preference. It can also be seen in the phase boundary maps in Fig. 14(a) that regions with OR-1 usually formed large contiguous blue regions but, when OR-2a and OR-2b were present, they tended to form as interwoven pink and yellow regions. This occurred because growth twinning of (Bi) in a region with OR-2a can result in a switching from OR-2a to OR-2b and vice versa, whereas twinning of (Bi) in a region of OR-1 maintains OR-1. For example, looking back at Fig. 11 on OR-2, there is one β-Sn orientation and two (Bi) orientations that are twinned, and the (Bi) twinning results in a change from OR-2a to OR-2b.

Past work on near-eutectic Sn-Bi alloys has shown that fully eutectic microstructures are promoted by low growth rates [22,53] and small undercoolings [24] and that β-Sn dendrites are promoted by higher growth rates [22] and deeper undercoolings [24], because the eutectic coupled zone is skewed to the side of the faceted (Bi) phase as is common in nonfaceted-faceted (nf-f) eutectics [53], including for solidification in an undercooled melt [24,54] taking into account kinetic undercooling effects [55,56]. Consistent with this, in this work, the fraction of β-Sn

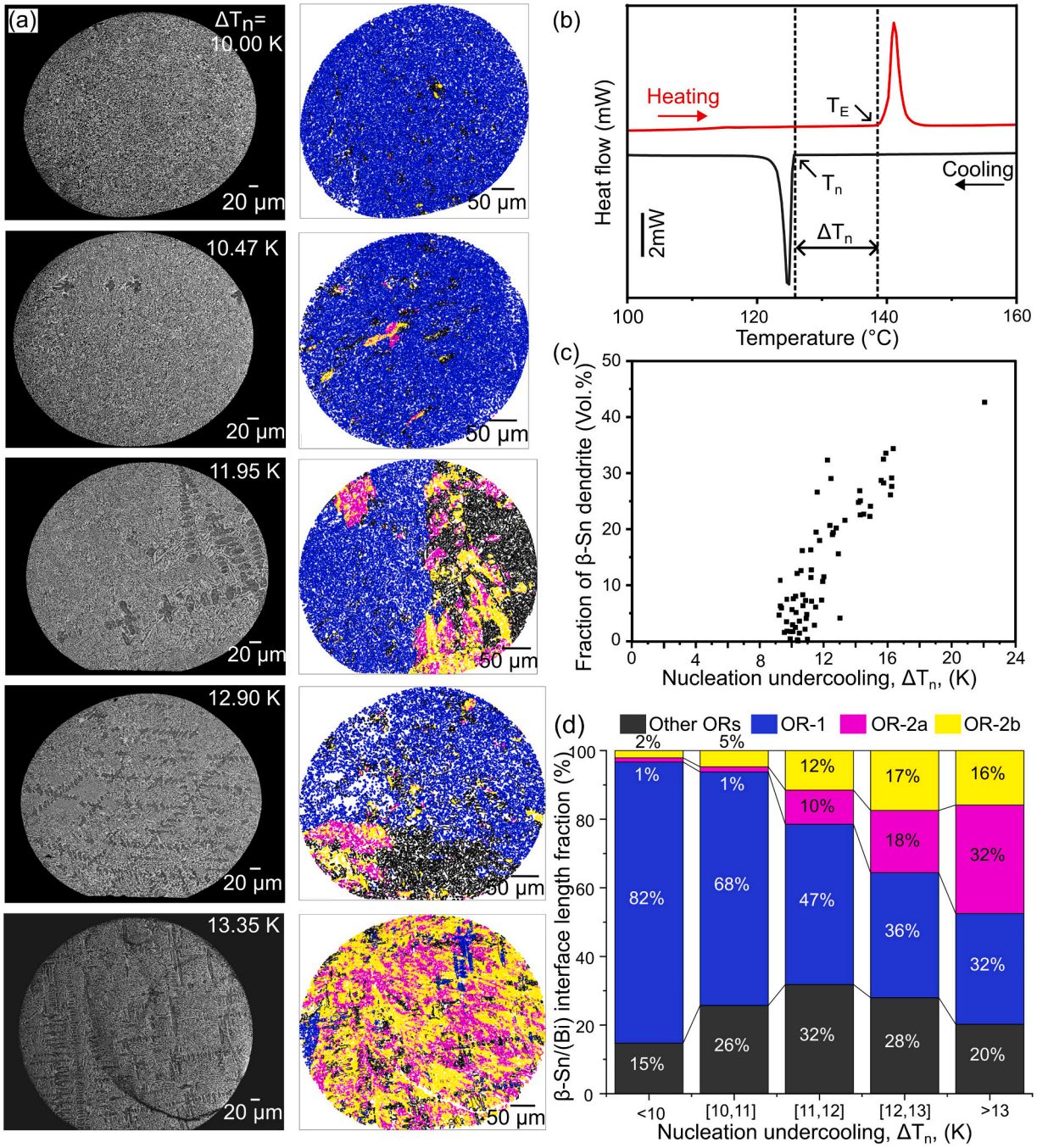


Fig. 14. Competition between eutectic ORs in the solidification of ~500 μm Sn-58Bi solder balls cooled at 20 K min^{-1} in a DSC. (a) Left column: BSE images with undercooling values annotated; Right column: phase boundaries plotted as: blue = OR-1, pink = OR-2a, yellow = OR-2b, black –other ORs. (b) Typical DSC thermogram, defining the nucleation undercooling, ΔT_n. (c) Measured fraction of β-Sn dendrites versus undercooling from 78 balls. (d) Stacked column chart of the fraction of each eutectic OR versus the undercooling. At least four solder balls were measured for each bin. Data from 32 solder balls are shown in total. ± 10° was used to define ORs.

dendrites in Sn-58Bi increased with deepening melt undercooling in DSC experiments as can be seen in the BSE images on the left of Fig. 14 (a) and is quantified in Fig. 14 (c). β-Sn nucleation typically occurred at/near the free surface as is common in droplet solidification when surface modification is not applied [57]. Thus, dendrites often grew inwards from the solder ball surface.

The effects of undercooling and prior β-Sn dendrite growth on the eutectic microstructure are examined in more detail in Fig. 15. Comparing the microstructures at $\Delta T_n = 10$ K with negligible β-Sn dendrites in Fig. 15 (a)-(e), versus at $\Delta T_n = 11.95$ K with clear β-Sn dendrites in Fig. 15 (g)-(l), multiple effects on eutectic growth are evident. β-Sn dendrites increased the fraction of (Bi) phase in the eutectic mixture, here from 49.4 area % (Bi) in Fig. 15 (a) to 53.8 area % in Fig. 15 (g), because dendrite growth enriches the remaining liquid in Bi solute. This change in eutectic phase fractions then impacts the phase interconnectivity: In (a), we see that β-Sn (the dark phase) is the more interconnected phase and can be considered the matrix of the eutectic whereas, in (g), the (Bi) phase is more interconnected. The pre-existing β-Sn dendrites also require the eutectic to continually change growth direction to grow around obstacles, and the eutectic interface velocity increases with deepening undercooling [56]. All four of these factors may influence the change in eutectic growth OR with deepening

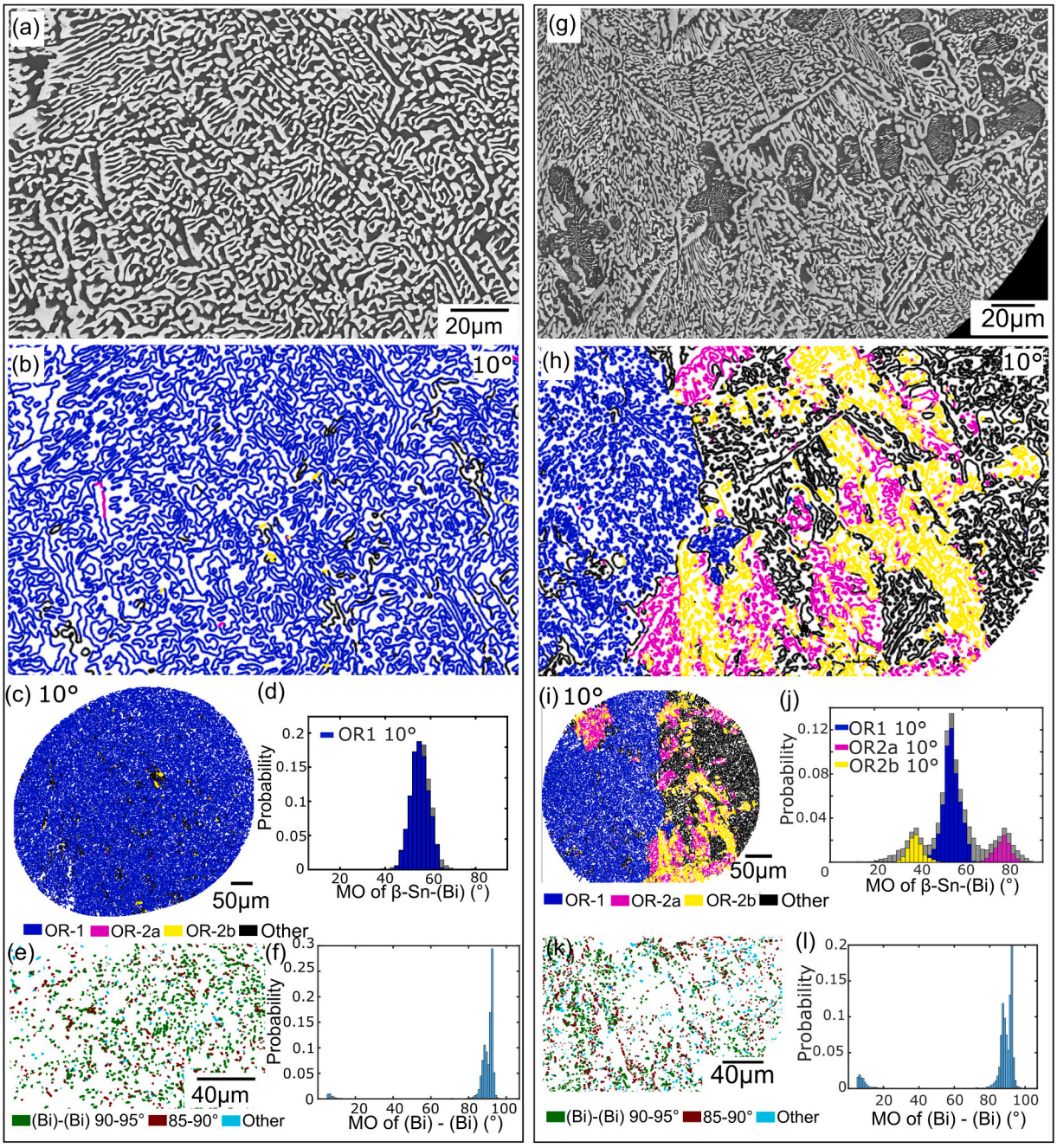


Fig. 15. Microstructure and interfaces in Sn-58wt%Bi solder balls. (a)-(f) a ball with $\Delta T_n = 10$ K. (g)-(l) a ball with $\Delta T_n = 11.95$ K. (a),(g) BSE images, (b), (h) phase boundary maps plotted with colours indicating the OR (or no OR) within ± 10°. (c), (i) low magnification phase boundary maps linking back to Fig. 14. (d), (j) β-Sn/(Bi) misorientation histograms with the three ORs ± 10° coloured. (e), (k) (Bi)-(Bi) interface maps plotted with colour to highlight the different twin types. (f), (k) (Bi)/(Bi) misorientation histograms containing a double peak at 87.6 and 92.4 ° corresponding to type I and II (Bi) twins.

undercooling and a dedicated study is required to explore this in detail.

The eutectic was generally less regular in solder balls that solidified in an undercooled melt than in unidirectional solidification into a positive temperature gradient. For example, comparing Fig. 15(a) and (g) with Fig. 10(a), there are fewer local areas with a regular fishbone structure in solder balls. Despite the less regular microstructure, there was only a slightly lower length fraction of β-Sn/(Bi) interfaces with an OR in solder balls (Fig. 14(d)) than in unidirectionally solidified samples (Fig. 13(e)). This shows that eutectic ORs were an important part of eutectic growth in undercooled solder balls, even when eutectic growth had to occur around pre-existing dendrites. Past work [58] on anomalous eutectic growth has shown that eutectic orientation relationships can be destroyed during solidification in undercooled melts, for example due to partial remelting during recalescence. In our work, eutectic ORs in Sn-Bi alloys were maintained at all undercoolings studied. However, since the undercoolings in this work were < 25 K, further work is required to test if ORs are destroyed at deeper undercooling.

The similarities between the ORs and interfaces in the undercooled solder balls and the unidirectionally solidified samples presented in Section 3.3 can be seen by comparing Fig. 15 (a)-(f) with Fig. 10, and more detailed examples are overviewed in Fig. 16. A subregion of the ball in Fig. 14(a) with $\Delta T_n = 10$ K is given in Fig. 16(a)-(e). There is a single β-Sn orientation and three main (Bi) orientations that are twinned, and all phase boundaries have OR-1, even though many parts of the

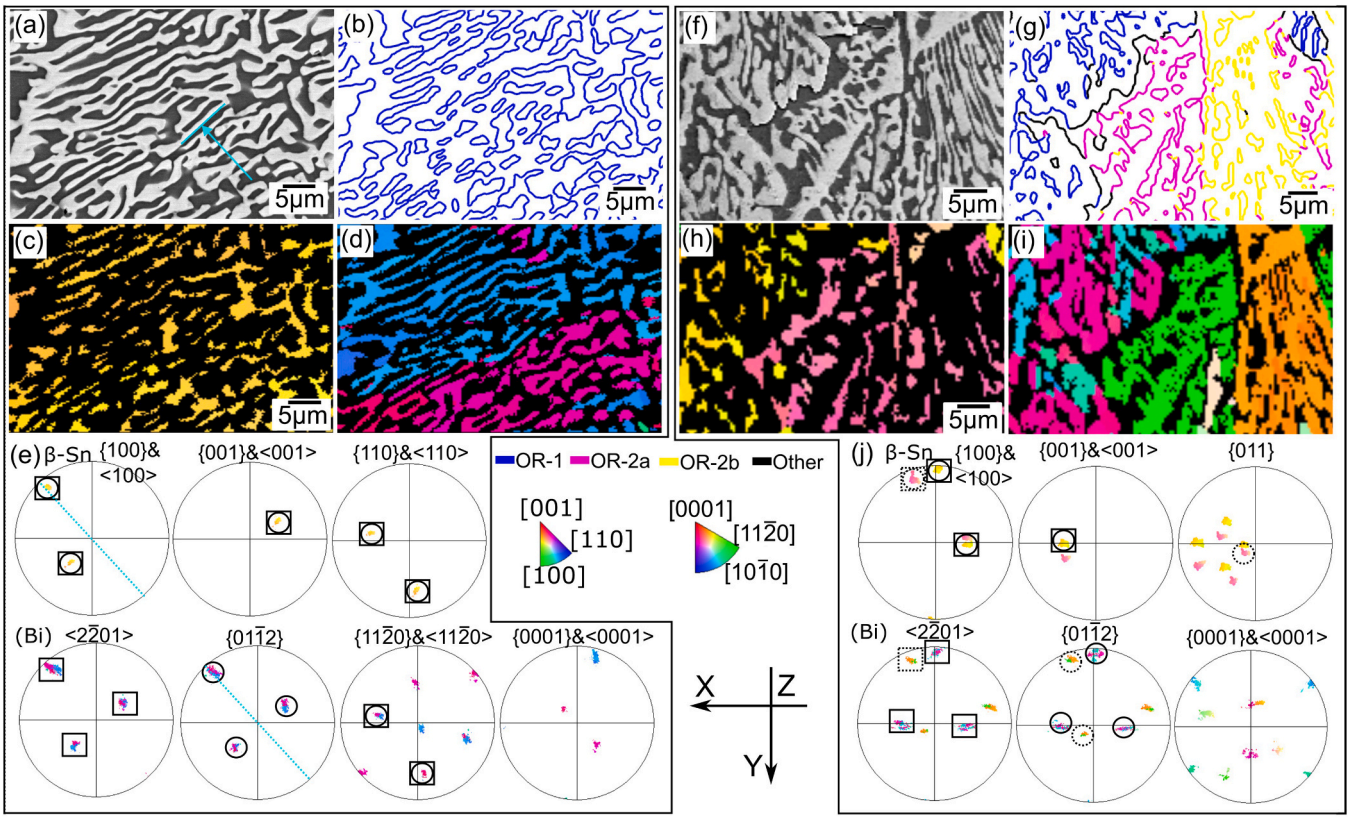


Fig. 16. OR analysis in Sn-58wt%Bi solder balls. (a)-(e) A subregion from a ball with $\Delta T_n = 10$ K. (f)-(j) A subregion from a ball with $\Delta T_n = 11.95$ K. (a), (f) BSE-SEM images. (b), (g) phase boundary maps plotted with colours indicating the OR (or no OR) within ± 10°. (c), (h) EBSD orientation maps of the β-Sn phase. (d), (i) EBSD orientation maps of the (Bi) phase. (e),(j) are selected pole figures for β-Sn (top) and (Bi) (bottom). Black circles indicate parallel planes. Black squares indicate parallel directions. Cyan lines in (e) indicate the interface plane normals annotated in cyan in (a).

boundaries are curved. In regions with relatively straight interfaces, these are often consistent with $\{01\bar{1}2\}_{(Bi)} \parallel \{100\}_{\beta-Sn}$. This can be confirmed from the annotated cyan arrow in Fig. 16(a) which indicates the projected interface plane normal, and the dashed cyan lines plotted as perpendicular bisectors on the pole figures in Fig. 16(e). A subregion of the ball in Fig. 14(c) with $\Delta T_n = 11.95$ K is given in Fig. 16(f)-(j). This eutectic region contains two β-Sn orientations (Fig. 16(h) and (j)). The top-left β-Sn orientation (yellow) has OR-1 to the cyan and pink (Bi) orientations (Fig. 16(g)-(j)). The bottom-right β-Sn orientation (pink) has OR-2a to the green and cream (Bi) orientations, and OR-2b to the orange (Bi) orientation (Fig. 16(g)-(j)). Fig. 16 confirms that the details of the ORs and interfaces in the undercooled solder balls were highly similar to the unidirectionally solidified samples presented in Section 3.3. This occurred despite the large differences in the solidification conditions in the two techniques including the well-controlled steady conditions in unidirectional solidification contrasting with the transient conditions in solder balls where the undercooling and gradients change during growth due to latent heat release in the undercooled melt.

The finding in Fig. 14 that the proportion of OR-2 increased as the melt undercooling became deeper suggests a potential method to control the eutectic OR and, therefore, the interfaces between β-Sn and (Bi) in Sn-58Bi solder joints. Past work on Sn-Ag-Cu solders has identified various methods to control undercooling during solder ball solidification (e.g. [48,59–62]) and future work could extend this to Sn-58Bi solder. Since the crack path in thermal fatigue is typically along β-Sn/(Bi) interfaces [18], future work could explore whether there are significant differences in the fracture behaviour when the β-Sn interface plane in the eutectic is {100} versus {101}, and undercooling control could potentially be used to tailor the interfaces via the eutectic ORs.

4. Conclusions

This study conducted a comprehensive analysis of eutectic orientation relationships between β-Sn and (Bi) in Sn-58Bi solder in two solidification conditions: 500 ± 15 μm diameter balls cooled in a DSC at 20 K/min with melt undercoolings in the range 8.8 < ΔT < 22 K, and unidirectional solidification of large samples at pulling rates from 0.5 – 40 μm/s. SEM-based and TEM-based diffraction techniques have been combined with crystallographic analyses to extract new insights into the crystallography of eutectic growth and the competition between different eutectic orientation relationships. The following conclusions can be drawn:

1. It has been found that eutectic (Bi) is often twinned with two twin types involving $\{10\bar{1}4\}$ and $\{01\bar{1}2\}$ twin planes.
2. Three reproducible β-Sn+ (Bi) eutectic orientation relationships have been identified that extend the original findings of Belyakov et al. [29]:

   OR-1: $\{100\}_{\beta-Sn} \parallel \{01\bar{1}2\}_{(Bi)}$ & $< 001 >_{\beta-Sn} \parallel < 2\bar{2}01>_{(Bi)}$ with the preferred direction $< 110 >$ and $< 11\bar{2}0 >$in the heat flow direction.

   OR-2a: $\{101\}_{\beta-Sn} \parallel \{01\bar{1}2\}_{(Bi)}$ & $< 010>_{\beta-Sn} \parallel < 2\bar{2}01>_{(Bi)}$

   OR-2b: $\{101\}_{\beta-Sn} \parallel \{10\bar{1}2\}_{(Bi)}$ & $< 010>_{\beta-Sn} \parallel < 2\bar{2}01>_{(Bi)}$

   Each orientation relationship involved multiple orientations of (Bi), resulting from the growth twinning of (Bi), each of which approximately had the OR to a single β-Sn orientation.
3. OR-1 was usually the dominant OR at steady-state in unidirectional solidification and in solder balls with small undercooling (≤ 10 K).

4. Deepening the melt undercooling has been found to increase the proportion of OR-2 and may offer a pathway to control the eutectic OR and, therefore, the β-Sn/(Bi) interfaces in electronic solder joints.

CRediT authorship contribution statement

James O. Douglas: Investigation. **Christopher M. Gourlay:** Writing – review & editing, Supervision, Resources, Conceptualization. **Xiaomei Shen:** Writing – original draft, Methodology, Investigation, Formal analysis. **Athanasios Zois:** Investigation.

Declaration of Competing Interest

The authors declare the following financial interests/personal relationships which may be considered as potential competing interests: James O. Douglas reports financial support was provided by EPSRC. If there are other authors, they declare that they have no known competing financial interests or personal relationships that could have appeared to influence the work reported in this paper.

Acknowledgements

The authors acknowledge use of characterization facilities within the Harvey Flower Electron Microscopy Suite, Department of Materials, Imperial College London. Cyro-Focused Ion Beam analysis was supported by the Henry Royce Institute for Advanced Materials at Imperial College London, funded through EPSRC Grant EP/X527257/1.

Appendix A. Supporting information

Supplementary data associated with this article can be found in the online version at doi:10.1016/j.jallcom.2025.181339.

References

[1] S. Sahasrabudhe *et al.*, Low temperature solder - A breakthrough technology for surface mounted devices, in *Proceedings - Electronic Components and Technology Conference*, Institute of Electrical and Electronics Engineers Inc., Aug. 2018, pp. 1455–1464. doi: 10.1109/ECTC.2018.00222.
[2] V. Jayaram, O. Gupte, K. Bhangaonkar, C. Nair, A review of low-temperature solders in microelectronics packaging, IEEE Trans. Compon. Packag. Manuf. Technol. 13 (4) (Apr. 2023) 570–579, https://doi.org/10.1109/TCPMT.2023.3271269.
[3] H. Fu *et al.*, iNEMI project on process development of BiSn-based low temperature solder pastes, in *In Proceedings of the 2017 SMTA International Conference*, Rosemont, Sep. 2017, pp. 207–220.
[4] S.A. Belyakov, C.M. Gourlay, Recommended values for the βSn solidus line in Sn-Bi alloys (no. February), Thermochim. Acta 654 (2017) 65–69, https://doi.org/10.1016/j.tca.2017.05.009.
[5] B.-J. Lee, C.-S. Oh, J.-H. Shim, Thermodynamic assessments of the Sn-ln and Sn-Bi binary systems, J. Electron Mater. 25 (6) (1996) 983–991.
[6] Y.A. Shen, et al., Sn-3.0Ag-0.5Cu/Sn-58Bi composite solder joint assembled using a low-temperature reflow process for PoP technology, Mater. Des. 183 (Dec. 2019), https://doi.org/10.1016/j.matdes.2019.108144.
[7] A. Luktuke, A.L. Kastengren, V. Nikitin, H. Torbati-Sarraf, N. Chawla, Bismuth pyramid formation during solidification of eutectic tin-bismuth alloy using 4D X-ray microtomography, Commun. Mater. 5 (1) (Dec. 2024), https://doi.org/10.1038/s43246-024-00538-9.
[8] R. Aspandiar, N. Badwe, and K. Byrd, Low Temperature Lead-Free Alloys and Solder Pastes, in *Lead-free Soldering Process Development and Reliability*, Bath. Jasbir, Ed., 2020, ch. 5, pp. 95–154. Accessed: Jan. 13, 2025. [Online]. Available: https://doi.org/10.1002/9781119482093.ch5.
[9] M. Ribas *et al.*, Low temperature soldering using Sn-Bi alloys, in *In Proceedings of SMTA International*, Rosemont, IL, USA, Sep. 2017, pp. 201–206.
[10] F. Wang, H. Chen, Y. Huang, L. Liu, Z. Zhang, Recent progress on the development of Sn–Bi based low-temperature Pb-free solders, J. Mater. Sci. Mater. Electron. 30 (4) (2019) 3222–3243, https://doi.org/10.1007/s10854-019-00701-w.
[11] S. Cheng, C.M. Huang, M. Pecht, A review of lead-free solders for electronics applications, Aug. 01, Elsevier Ltd, 2017, https://doi.org/10.1016/j.microrel.2017.06.016.
[12] G. Ren, I.J. Wilding, M.N. Collins, Alloying influences on low melt temperature SnZn and SnBi solder alloys for electronic interconnections, J. Alloy. Compd. 665 (2016) 251–260, https://doi.org/10.1016/j.jallcom.2016.01.006.
[13] L. Shen, P. Lu, S. Wang, Z. Chen, Creep behaviour of eutectic SnBi alloy and its constituent phases using nanoindentation technique, J. Alloy. Compd. 574 (2013) 98–103, https://doi.org/10.1016/j.jallcom.2013.04.057.
[14] N. Badwe, K. Byrd, O. Jin, P. Goonetilleke, Tin-Bisumth low temperature homogeneous second level interconnect solder joint microstructure, reliability, and failure mechanism, Proc. SMTA Int. (2019) 507–512.
[15] O.H. Chen, et al., Mechanical shock and drop reliability evaluation of the BGA solder joint stack-ups formed by reflow soldering SAC solder balls BGAs with BiSnAg and resin reinforced BiSn-based solder pastes, Proc. SMTA Int. (2015) 215–222.
[16] H.N. Fowler, et al., Effect of Sb and Ag addition and aging on the microstructural evolution, IMC layer growth, and mechanical properties of near-eutectic Sn-Bi alloys, J. Electron Mater. 53 (3) (Mar. 2024) 1284–1298, https://doi.org/10.1007/s11664-023-10866-0.
[17] P. Choudhury, M. Ribas, R.R. Rangaraju, S. Sarkar, M. Alpha, E. Solutions, High reliability low temperature solder alloys, Proc. SMAT Int. (2019) 526–531.
[18] K. Young, R. Aspandiar, N. Badwe, S. Walwadkar, Y.W. Lee, T.K. Lee, Thermal cycling induced interconnect stability degradation mechanism in low melting temperature solder joints, Proc. - Electron. Compon. Technol. Conf. Inst. Electr. Electron. Eng. Inc. (May 2022) 1199–1205, https://doi.org/10.1109/ECTC51906.2022.00192.
[19] B.L. Silva, G. Reinhart, H. Nguyen-Thi, N. Mangelinck-Noël, A. Garcia, J.E. Spinelli, Microstructural development and mechanical properties of a near-eutectic directionally solidified Sn-Bi solder alloy, Mater. Charact. 107 (2015) 43–53, https://doi.org/10.1016/j.matchar.2015.06.026.
[20] S.D. Bagheri, J.W. Rutter, Origin of microstructure in Bi-Pb and Bi-Sn binary eutectics, Mater. Sci. Technol. 13 (7) (1997) 541–550, https://doi.org/10.1179/mst.1997.13.7.541.
[21] E. Çadırlı, H. Kaya, N. Maraşlı, The dependence of lamellar spacings and microhardness on the growth rate in the directionally solidified Bi-43 wt% Sn alloy at a constant temperature gradient, Met. Mater. Int. 15 (5) (2009) 741–751, https://doi.org/10.1007/s12540-009-0741-5.
[22] M.J. Suk, G.H. Choi, I.H. Moon, Formation of halo in Sb-InSb and Sn-Bi eutectic alloy systems, J. Cryst. Growth 123 (1–2) (1992) 5–16, https://doi.org/10.1016/0022-0248(92)90005-4.
[23] M.N. Croker, M. McParlan, D. Baragar, R.W. Smith, Anomalous eutectic growth. I. The determination of the eutectic structures of Bi-T1Bi2, Bi-Sn, Sb-Pb and Sb-InSb using an accelerated growth technique, J. Cryst. Growth 29 (1) (1975) 85–97, https://doi.org/10.1016/0022-0248(75)90055-X.
[24] M.F.X. Gigliotti, G.L.F. Powell, G.A. Colligan, A temperature-composition zone of coupled eutectic growth in the Sn-Bi system, Metall. Trans. 1 (4) (1970) 1038–1041, https://doi.org/10.1007/BF02811795.
[25] H.W. Kerr, W.C. Winegard, The structures of the Bi-Sn, Bi-Pb and Bi-Ti eutectics, Can. Metall. Q. 6 (1) (1967) 55–65, https://doi.org/10.1179/cmq.1967.6.1.55.
[26] A.M. Delhaise, D.D. Perovic, Study of solid-state diffusion of bi in polycrystalline sn using electron probe microanalysis, J. Electron Mater. 47 (3) (2018) 2057–2065, https://doi.org/10.1007/s11664-017-6011-x.
[27] J.M. Juarez, et al., Manufacturability and reliability screening of lower melting point, Pb-free alloys containing bismuth, J. Microelectron. Electron. Packag. 12 (1) (2015) 1–28, https://doi.org/10.4071/imaps.441.
[28] A.M. Delhaise, et al., Thermal preconditioning and restoration of bismuth-containing, lead-free solder alloys, J. Electron Mater. 49 (1) (2020) 116–127, https://doi.org/10.1007/s11664-019-07666-w.
[29] S.A. Belyakov, et al., Precipitation and coarsening of bismuth plates in Sn–Ag–Cu–Bi and Sn–Cu–Ni–Bi solder joints, J. Mater. Sci. Mater. Electron. 30 (1) (2019) 378–390, https://doi.org/10.1007/s10854-018-0302-8.
[30] J.A. Wu, A. Luktuke, N. Chawla, Surface precipitation and growth of bismuth particles in Sn-Ag-Cu-Bi solder joints, J. Electron Mater. 52 (2) (Feb. 2023) 801–809, https://doi.org/10.1007/s11664-022-10126-7.
[31] P. Hofmann, The surfaces of bismuth: structural and electronic properties, Prog. Surf. Sci. 81 (5) (2006) 191–245, https://doi.org/10.1016/j.progsurf.2006.03.001.
[32] F. Jona, Low-energy electron diffraction study of surfaces of antimony and bismuth, Surf. Sci. 8 (1–2) (Jul. 1967) 57–76, https://doi.org/10.1016/0039-6028(67)90073-8.
[33] M.C. Allison, M. Avdeev, S. Schmid, S. Liu, T. Söhnel, C.D. Ling, Synthesis, structure and geometrically frustrated magnetism of the layered oxide-stannide compounds Fe(Fe3-XMnx)Si2Sn7O16, Dalton Trans. 45 (23) (2016) 9689–9694, https://doi.org/10.1039/c6dt01074a.
[34] P. Cucka, C.S. Barrett, The crystal structure of Bi and of solid solutions of Pb, Sn, Sb and Te in Bi, Acta Crystallogr 15 (9) (1962) 865–872.
[35] F. Wang, A. Luktuke, N. Chawla, Microstructural coarsening and mechanical properties of eutectic Sn-58Bi solder joint during aging, J. Electron Mater. 50 (12) (Dec. 2021) 6607–6614, https://doi.org/10.1007/s11664-021-09255-2.
[36] R. Elliott, Eutectic solidification, Int. Met. Rev. 22 (1) (Jan. 1977) 161–186, https://doi.org/10.1179/imtr.1977.22.1.161.
[37] A.I. Pinchuk, S.D. Shavrei, Threshold character of the magnetoplastic effect in twinning of bismuth crystals, Defects Dislocations Phys. Strength 9 (Dec. 2003) 1603–1606.
[38] W.F. Berg, Mechanical twinning in bismuth crystals, Nature 133 (3370) (Jun. 1934) 831–832, https://doi.org/10.1038/133831a0.
[39] O.M. Ostrikov, Twinning in bismuth single crystals induced by thermal cycling, Tech. Phys. 46 (9) (Sep. 2001) 1199–1201, https://doi.org/10.1134/1.1404177.
[40] Y. Yanaka, Y. Kariya, H. Watanabe, H. Hokazono, Plastic deformation behavior and mechanism of bismuth single crystals in principal axes, Mater. Trans. 57 (6) (2016) 819–823, https://doi.org/10.2320/matertrans.MD201503.

[41] A.I. Pinchuk, S.D. Shavrei, Magnetoplastic effect in twinning of bismuth crystals under a concentrated load, Phys. Solid State 43 (Jan. 2001) 39–41.
[42] Y. Yanaka, Y. Kariya, H. Watanabe, H. Hokazono, Influence of temperature on plastic deformation behavior and mechanism of bismuth single crystals, J. Electron Mater. 47 (1) (Jan. 2018) 594–603, https://doi.org/10.1007/s11664-017-5804-2.
[43] S. Sun, C.M. Gourlay, Dendrite growth in single-grain and cyclic-twinned Sn–3Ag–0.5Cu solder joints, Metall. Mater. Trans. A 55 (11) (Nov. 2024) 4342–4353, https://doi.org/10.1007/s11661-024-07580-9.
[44] O.'hara S, Web-dendrite growth of single crystals of tin, J. Cryst. Growth 1 (1967) 73–78, https://doi.org/10.1016/0022-0248(67)90012-0.
[45] J.C. Warner, J.D. Verhoeven, Morphology of tin dendrites in near-eutectic alloys, Metall. Trans. 3 (4) (Apr. 1972) 1001–1002, https://doi.org/10.1007/BF02647678.
[46] F. Weinberg, B. Chalmers, Further observations on dendritic growth in metals, Can. J. Phys. 30 (5) (1952) 488–502.
[47] Z.L. Ma, C.M. Gourlay, Nucleation, grain orientations, and microstructure of Sn-3Ag-0.5Cu soldered on cobalt substrates, J. Alloy. Compd. 706 (2017) 596–608, https://doi.org/10.1016/j.jallcom.2017.02.243.
[48] Z.L. Ma, S.A. Belyakov, K. Sweatman, T. Nishimura, T. Nishimura, C.M. Gourlay, Harnessing heterogeneous nucleation to control tin orientations in electronic interconnections, Nat. Commun. 8 (1) (Dec. 2017), https://doi.org/10.1038/s41467-017-01727-6.
[49] B.L. Bramfitt, The effect of carbide and nitride additions on the heterogeneous nucleation behavior of liquid iron, Metall. Trans. 1 (10) (1970) 2958, https://doi.org/10.1007/BF03037838.
[50] S.A. Belyakov, C.M. Gourlay, Heterogeneous nucleation of βSn on NiSn4, PdSn4 and PtSn4, Acta Mater. 71 (Jun. 2014) 56–68, https://doi.org/10.1016/j.actamat.2014.02.044.
[51] Z.L. Ma, H. Shang, A.A. Daszki, S.A. Belyakov, C.M. Gourlay, Mechanisms of beta-Sn nucleation and microstructure evolution in Sn-Ag-Cu solders containing titanium, J. Alloy. Compd. 777 (Mar. 2019) 1357–1366, https://doi.org/10.1016/j.jallcom.2018.11.097.
[52] Z.L. Ma, J.W. Xian, S.A. Belyakov, C.M. Gourlay, Nucleation and twinning in tin droplet solidification on single crystal intermetallic compounds, Acta Mater. 150 (May 2018) 281–294, https://doi.org/10.1016/j.actamat.2018.02.047.
[53] W. Kurz, D.J. Fisher, Dendrite growth in eutectic alloys: the coupled zone, Int. Met. Rev. 24 (1) (Jan. 1979) 177–204, https://doi.org/10.1179/imtr.1979.24.1.177.
[54] M.X. Li, H.P. Wang, M.J. Lin, C.H. Zheng, B. Wei, Rapid eutectic growth kinetics of undercooled Nb-Si alloys at electrostatic levitation state, Acta Mater. 237 (Sep. 2022), https://doi.org/10.1016/j.actamat.2022.118157.
[55] C. Yang, J. Gao, Modeling of free eutectic growth and competitive solidification in undercooled near-eutectic alloys based on in situ measurements, J. Mater. Sci. 50 (1) (Jan. 2015) 268–278, https://doi.org/10.1007/s10853-014-8585-5.
[56] J.F. Li, Y.H. Zhou, Eutectic growth in bulk undercooled melts, Acta Mater. 53 (8) (May 2005) 2351–2359, https://doi.org/10.1016/j.actamat.2005.01.042.
[57] J.H. Perepezko, G. Wilde, Melt undercooling and nucleation kinetics, Curr. Opin. Solid State Mater. Sci. 20 (2016) 3–12. ⟨https://www.elsevier.com/open-access/userlicense/1.0/⟩ ([Online]. Available).
[58] X.X. Wei, et al., Remelting-induced anomalous eutectic formation during solidification of deeply undercooled eutectic alloy melts, Acta Mater. 95 (Jun. 2015) 44–56, https://doi.org/10.1016/j.actamat.2015.05.014.
[59] S.K. Kang, et al., Controlling Ag 3 Sn plate formation in near-ternary-eutectic Sn-Ag-Cu solder by minor Zn alloying, JOM (Jun. 2004) 34–38.
[60] I.E. Anderson, J.W. Walleser, J.L. Harringa, F. Laabs, A. Kracher, Nucleation control and thermal aging resistance of near-eutectic Sn-Ag-Cu-X solder joints by alloy design, J. Electron Mater. 38 (12) (Dec. 2009) 2770–2779, https://doi.org/10.1007/s11664-009-0936-7.
[61] M.G. Cho, H.Y. Kim, S.K. Seo, H.M. Lee, Enhancement of heterogeneous nucleation of B -Sn phases in Sn-rich solders by adding minor alloying elements with hexagonal closed packed structures, Appl. Phys. Lett. 95 (2) (2009), https://doi.org/10.1063/1.3177335.
[62] H. Shang, Z.L. Ma, S.A. Belyakov, C.M. Gourlay, Grain refinement of electronic solders: the potential of combining solute with nucleant particles, J. Alloy. Compd. 715 (2017) 471–485, https://doi.org/10.1016/j.jallcom.2017.04.268.